Global and Planetary Change 228 (2023) 104213

Contents lists available at ScienceDirect

Global and Planetary Change

journal homepage: www.elsevier.com/locate/gloplacha

The development of ocean currents and the response of the cryosphere on the Southwest Svalbard shelf over the Holocene

Dhanushka Devendra [a,*], Magdalena Łącka [a], Natalia Szymańska [a], Małgorzata Szymczak-Żyła [a], Magdalena Krajewska [a], Agnes K.M. Weiner [b], Stijn De Schepper [b], Margit Hildegard Simon [b], Marek Zajączkowski [a]

[a] Department of Paleoceanography, Institute of Oceanology, Polish Academy of Sciences, Sopot 81-712, Poland
[b] NORCE Climate and Environment, NORCE Norwegian Research Centre AS and Bjerknes Centre for Climate Research, Bergen, Norway

ARTICLE INFO

Editor: Dr. Fabienne Marret-Davies

Keywords:
Arctic
Hornsund
Atlantic Water
Arctic Water
Foraminifera
Stable isotopes
Biomarker
Holocene

ABSTRACT

While general trends in the inflow of Atlantic Water (AW) to the European Arctic over the present interglacial (the Holocene) are well known, regional changes in climate and the AW current and subsequent environmental responses are less well established. In particular, there is only limited knowledge on the development of ocean currents after the last deglaciation. Here, to better understand past water mass dynamics and their effects on sea ice cover and the environment throughout the Holocene, we present a multiproxy record from core OCE2019-HR7-GC retrieved from the southwestern Svalbard inner shelf, a highly dynamic frontal area influenced by different ocean currents and local water masses. For sea ice reconstructions, we focus on the specific sea ice biomarker IP_{25} in combination with the phytoplankton biomarkers dinosterol and brassicasterol. We further reconstruct surface and bottom water temperatures using alkenones and Mg/Ca and prevailing water masses using foraminifera assemblages. Finally, we compare our sea ice and temperature records with published marine sediment and ice core data from the area. We observe extensive sea ice cover between 11 and 10.2 kyr BP, which was likely linked to the Preboreal Oscillation. Based on our reconstructions, the period between 10 and 7 kyr BP was characterized by the warmest Holocene conditions on the SW Svalbard shelf. This interval is also associated with high surface water productivity and an enhanced AW influx that drove strong erosive activity at the bottom. After 6.5 kyr BP, the SW Svalbard shelf was characterized by a dynamic environment with cold and unstable conditions that lasted until 3.5 kyr BP. After 3.5 kyr BP, we observed an increase in sea ice cover and iceberg rafting over our site once more, which likely indicated seasonally fluctuating ice margins, with low AW influx, which lasted until 2.2 kyr BP. A brief warm period accompanied by strong bottom currents occurred between 2.2 and 1.8 kyr BP. The environment returned to a colder state with the presence of sea ice until 1.5 kyr BP, which was followed by warmer conditions between 1.5 and 1 kyr BP.

1. Introduction

Over the last decade, northern latitudes have received increased attention within the context of ongoing global warming. This is motivated by rising global sea levels due to the melting of Arctic glaciers and some extreme events, such as the 2012 sea ice minimum. Several studies have revealed that the Arctic warming rate is twice as high as the world average (Screen and Simmonds, 2010; Serreze et al., 2009) due to rapid sea ice loss, which is a phenomenon known as Arctic amplification (Cohen et al., 2014; Serreze and Barry, 2011). Sea ice becomes thinner as it melts, making it easier for the area to absorb more solar energy, which results in extra heating.

The climate in the European Arctic is strongly dependent on the inflow of warm and saline Atlantic Water (AW) transported to the high northern latitudes by the North Atlantic Current (NAC). The West Spitsbergen Current (WSC), the furthest branch of the NAC, is thought to be the main pathway for the flux of heat, salt, and water into the Arctic Ocean (Aagaard and Greisman, 1975; Skogseth et al., 2005); hence, the West Spitsbergen continental margin is climatically sensitive area. The strength of AW influx into the northern North Atlantic has changed throughout the Holocene, though the amplitude of the change is smaller than the changes that occurred on glacial-interglacial scales (e.g., Hald

* Corresponding author.
E-mail address: devendra@iopan.pl (D. Devendra).

https://doi.org/10.1016/j.gloplacha.2023.104213
Received 22 March 2023; Received in revised form 4 August 2023; Accepted 11 August 2023
Available online 12 August 2023

et al. (2007)).

The paleoceanographic changes during the Holocene have been documented for high latitude North Atlantic and adjacent Barents Sea. The entire region has been directly affected by warm AW advection (Łącka et al., 2015a; Lubinski et al., 2001; Rasmussen et al., 2014; Rasmussen et al., 2007; Risebrobakken et al., 2011; Sarnthein et al., 2003; Ślubowska-Woldengen et al., 2007; Ślubowska et al., 2005). These studies indicate significant variations in sea water temperature, sea ice and the strength of the surface and deep water currents over the Holocene. After the cold Younger Dryas, the inflow of warm AW to the North Atlantic and Barents Sea increased (e.g., Hald et al., 2007; Łącka et al., 2015a; Rasmussen et al., 2007; Ślubowska-Woldengen et al., 2008). This AW inflow combined with the increased Holocene summer insolation (Berger and Loutre, 1991) caused the significant increase in sea surface temperatures (SSTs) (e.g., Belt et al., 2015; Łącka et al., 2015a). These warmer conditions resembling the Holocene Thermal Maximum (HTM) are seen throughout this region, where sea ice free conditions remained between 10 and 6 kyr BP (e.g., Calvo et al., 2002; Łącka et al., 2015a; Risebrobakken et al., 2011). However, a number of paleo surface ocean temperature reconstructions based on diatoms (e.g., Andersen et al., 2004; Birks and KoÇ, 2008), alkenones (e.g., Calvo et al., 2002; Łącka et al., 2019) and planktic foraminifera (e.g., Berben et al., 2014; Sarnthein et al., 2003) show a different timing of HTM. Furthermore, studies of marine sediment cores collected from the region reveal that both short- and long-term climatic changes, such as the transition from the warm early Holocene to the cool and stable mid-Holocene, can be attributed to variations in AW flow and to the oceanic conveyor belt in addition to variability in insolation (Ebbesen et al., 2007; Knies et al., 2016; Rasmussen and Thomsen, 2015; Rasmussen et al., 2007; Ślubowska et al., 2005).

Previous studies of the western Svalbard area have focused on water mass changes and their impact on the environment during the Holocene, but did not provide a detailed understanding of the mechanisms controlling sea ice cover and its dynamics. This study reveals the development of the Holocene palaeoenvironment within the inner SW Svalbard shelf by examining the physical properties of the sediment, the faunal distribution and geochemical composition of benthic foraminifera, and biomarkers. The study site is a natural sediment trap and covers the entire Holocene within 230 cm of sediments, allowing for a sampling resolution at decadal to centennial timescales. Here, we focus especially on (1) the effect of the interplay between warm AW, Arctic water, and cold local water from the inner Hornsund on the dynamics of ice coverage and (2) how these changes affected the local and regional climate and ocean during the Holocene. To achieve a more comprehensive understanding of regional developments, we compared our records with other studies conducted in the western Barents Sea (Berben et al., 2014; Łącka et al., 2019) and SW Svalbard (Sternal et al., 2014; Telesiński et al., 2018).

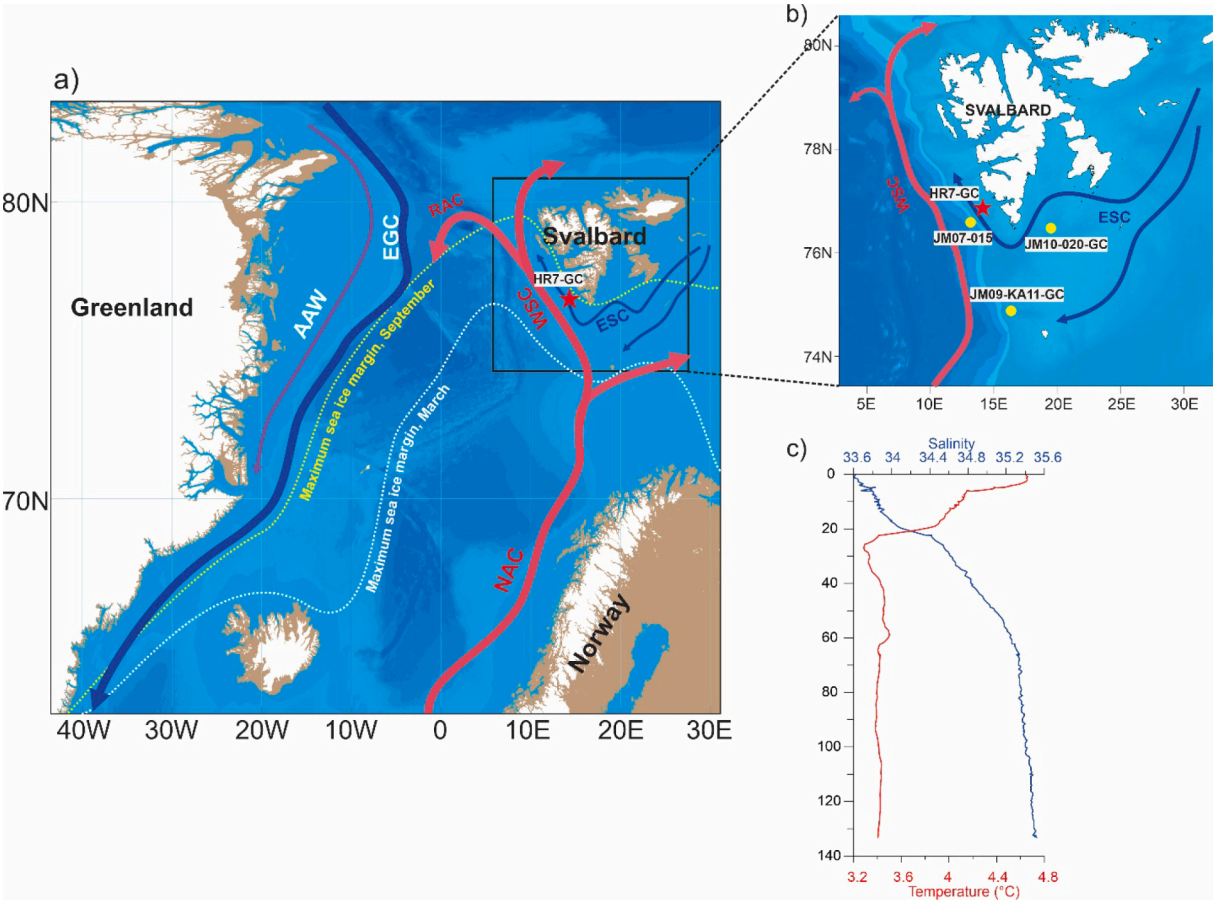

Fig. 1. (a) Map of the coring site and schematic of present-day surface ocean circulation in the Nordic Seas. The red arrows represent the flow of warm Atlantic Water, i.e., North Atlantic Current (NAC), West Spitsbergen Current (WSC), and Return Atlantic Current (RAC). The dashed blue arrow represents the East Spitsbergen Current (ESC), and the dashed purple arrow represents Arctic Atlantic Water (AAW). The blue arrow denotes the East Greenland Current (EGC). Dashed lines show the average winter maximum (March; white) and summer maximum (September; yellow) sea ice margins in the period 1972–2007 (Fetterer and Fowler, 2006). (b) Bathymetry map of the Svalbard shelf and location of the studied sediment core OCE2019-HR7-GC (red star). Locations of marine sediment cores mentioned in the text are shown by yellow circles: JM07–015 (Sternal et al., 2014), JM10–020-GC (Łącka et al., 2019), and JM09-KA11-GC (Berben et al., 2014). (c) Salinity, temperature, and depth profiles measured in August 2019 at the core site of OCE2019-HR7-GC (temperature in red and salinity in blue). (For interpretation of the references to colour in this figure legend, the reader is referred to the web version of this article.)

2. Regional setting

The study area is located on the shelf outside of Hornsund fjord (Fig. 1) and is dominated by two northwards propagating currents, the WSC and the East Spitsbergen Current (ESC) (also called the Sørkapp Current). The WSC carries warm and saline AW ($T > 3$ °C, S > 35.0), is steered by the topography and flows into the Arctic Ocean along the western coast of Svalbard. Along the continental slope of Svalbard, the warm core of the WSC loses 1050 Wm^{-2} of heat in winter and 330 Wm^{-2} in summer (Saloranta and Haugan, 2004). The ESC is generally restricted to the Svalbard continental shelf and transports a mixture of relatively fresh, cold Arctic Water (ArW, $T < 3$ °C, S < 35.0) and drift ice from the Barents Sea. The Arctic front marks the boundary between WSC and ESC at the shelf edge (Loeng, 1991; Saloranta and Svendsen, 2001). However, these two water masses (AW and ArW) are mixed in most of the Western Spitsbergen shelf areas and are referred to as Transformed Atlantic Water.

3. Materials and methods

The gravity core OCE2019-HR7-GC (76°56.513 N, 14°54.072E; hereafter HR7) was obtained during the AREX expedition with the RV Oceania in 2019 from 133 m water depth on the continental shelf at the entrance to Hornsund fjord (Fig. 1). The water column temperature and salinity at the coring site were measured in situ using a mini-CTD (conductivity–temperature–depth) profiler, which sampled at 1 s intervals. A seismic survey was carried out using an Innomar SES-200 Deep, sub-bottom profiler before core collection to select a suitable location for coring. The sediment core was stored at 4 °C and transported to the Institute of Oceanology PAS for further analysis. Before opening, the core was scanned using a medical X-ray computed tomography (CT) scanner. The colour and structure of the sediment core were described soon after opening. The 2.32 m long core was sampled into 1 cm slices. Samples were weighed, freeze-dried, and weighed again, and the water content was calculated (Fig. 2).

3.1. Chronology

The chronology of core HR7 is based on ten AMS ^{14}C dates taken from the benthic foraminifera *Cibicidoides lobatulus* and dated at the MICADAS facility at the Alfred-Wegener Institute in Bremerhaven, Germany. The resulting AMS ^{14}C dates were calibrated to calendar ages using the Marine20 calibration curve (Heaton et al., 2020) in CALIB 8.2.0 (Stuiver et al., 2022), and local reservoir correction was applied

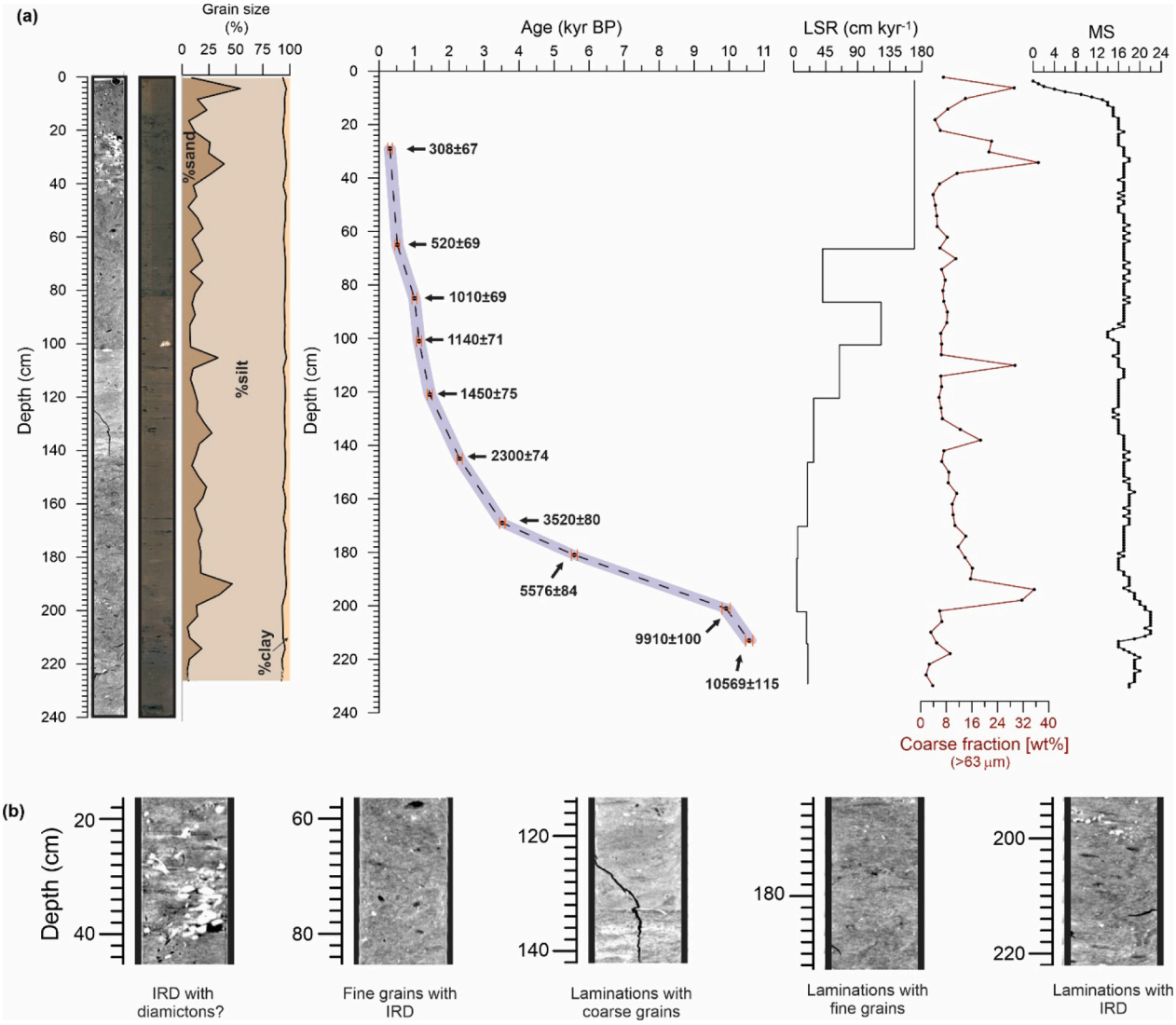

Fig. 2. (a) Lithology and age-depth model of core OCE2019-HR7-GC. Computer tomography and core scan images, grain size distribution, age-depth model, linear sedimentation rates (LSR), coarse fraction (>63 μm), and magnetic susceptibility (MS). (b) Visible changes in sediment deposition are highlighted in the image from the CT scan.

(ΔR = 105 ± 24) (Mangerud et al., 2006). We are well aware of the statement of Heaton et al. (2020) that Marine20 is not suitable for use in higher latitudes, where variations in sea-ice extent, ocean upwelling, and air-sea gas exchange may have create uncertainty with the reservoir age. Nevertheless, this uncertainty is not resolved by using an older version of the calibration dataset (e.g. Marine13). However, Marine13 has been widely used for higher latitudes paleoceanography e.g. (Łącka et al., 2019). Since its release, Marine20 also has seen much application in higher latitudes (Devendra et al., 2022; Pieńkowski et al., 2021), and thus we used the Marine20 dataset to calibrate radiocarbon ages for this study. Calibrated ages have been interpolated, assuming linear sedimentation rates between dated points. The core top was also dated using bivalve shells and obtained age shows modern age (Table 1). The age obtained 17 cm within HR7 is older than the date from 29 cm (Table 1). The older date was therefore excluded from the age model since this age reversal may have resulted from the reworking of older specimens of *C. lobatulus* at the site.

3.2. X-ray fluorescence and magnetic susceptibility scanning

X-ray fluorescence (XRF) scanning of the sediment core was conducted at the Department of Earth Science, University of Bergen, Norway with an ITRAX XRF core scanner equipped with a molybdenum X-ray tube at 30 kV and 30 mA to record the elemental spectra at 2 mm resolution. The magnetic susceptibility was measured at 1 cm intervals using a GEOTEK Multi-Sensor Core Logger (MSCL-S). Element ratios, rather than individual elements, are used to prevent closed-sum effects, and Br and Rb were normalized using Ti as generally used in geochemical studies for normalization.

3.3. Organic bulk sediment parameters and IRD

The total carbon (TC) and total organic carbon (TOC) were measured on homogenized bulk sediment samples using the combustion technique with chromatographic detection, performed with a Flash 2000 elemental analyser by Thermo at Ecotech Lab (Gdansk, Poland). For TC analyses, samples were analysed without pretreatment. TOC was determined after removing carbonates via acidification of the sample with hydrochloric acid. The carbonate content ($CaCO_3$) was calculated according to TOC and TC values using the following equation.

$$CaCO_3 = (TC - TOC) \times 100/12$$

Ice-rafted debris (IRD) was counted in the >500 μm size fraction. Fluxes and the concentration of IRD per sample were calculated. At least 200 mineral grains per sample were counted.

Table 1
AMS ^{14}C measurements and calibrated ages from the Marine20 calibration curve. Median ages (in bold) were used for the age-depth model. Calibrated ages are reported in thousands of years before 1950 CE (kyr BP).

Lab ID	Depth (cm)	Dated material	^{14}C age (year BP)	Calibrated age (year BP, 2σ)		
				Min age	Max age	Median age
01–01-49	1	Bivalve	Modern age	–	–	–
8189.1.1	17	*C. lobatulus*	1187 ± 65*	Excluded		
8190.1.1	29	*C. lobatulus*	958 ± 67	115	492	**308**
8191.1.1	65	*C. lobatulus*	1200 ± 69	343	673	**520**
8192.1.1	85	*C. lobatulus*	1733 ± 69	823	1230	**1010**
8193.1.1	101	*C. lobatulus*	1843 ± 71	932	1304	**1140**
8941.1.1	121	*C. lobatulus*	2170 ± 75	1280	1687	**1450**
8194.1.1	145	*C. lobatulus*	2838 ± 74	2012	2529	**2300**
8942.1.1	169	*C. lobatulus*	3870 ± 80	3310	3807	**3520**
8195.1.1	181	*C. lobatulus*	5498 ± 84	5323	5811	**5576**
8943.1.1	201	*C. lobatulus*	9399 ± 100	9571	10,189	**9910**
9186.1.1	213	*C. lobatulus*	9892 ± 115	10,364	10,748	**10,569**

* The radiocarbon age from 17 cm was excluded from the age-depth model

3.4. Foraminifera analysis

We conducted a thorough analysis of foraminifera every fourth centimeter, except for the 189 to 205 cm interval, where we analysed every two centimeters. In total, we analysed 62 samples. The samples were weighed, freeze-dried, weighed again and then wet sieved over a 63 μm, 100 μm, and 500 μm fractions and dried at 50 °C. A minimum of 300 benthic foraminiferal specimens from the >100 μm fraction of each sample were picked under the light microscope. When necessary, residues were split using a dry microsplitter, and the total number of foraminifera was calculated. The taxonomic classification was performed mostly at the species level, using the generic classification of Loeblich Jr and Tappan (2015). Relative abundances of individual taxa and fluxes of total benthic foraminifera and individual taxa (specimens cm^{-2} kyr^{-1}) were calculated using linear sedimentation rates (LSRs). The individual abundances of planktic foraminifera taxa were very low and excluded from the detailed analysis. However, we counted the total planktic foraminifera, and total planktic fluxes were calculated by using LSR.

The foraminiferal fluxes were calculated using the following formula:

$$\text{Flux}\left(\text{individuals} \times \text{cm}^{-2} \times \text{kyr}^{-1}\right) = \text{FN} \times \rho \times \text{LSR}$$

where FN is the foraminifera number (per gram dry sediment) [individuals g^{-1}], ρ is the density of dry sediment [g cm^{-3}], and LSR is the linear sedimentation rate [cm kyr^{-1}].

3.5. Stable isotopes

The benthic foraminifera species *Elphidium clavatum* was used for the stable carbon and oxygen isotope analysis. Twenty-five specimens were picked from the 100–500 μm size fraction of each analysed sample. All of the stable isotope analyses were performed using a Thermo Finnigan MAT 252 mass spectrometer with a Kiel III automatic carbonate preparation device at the Light Stable Isotope Mass Spec Laboratory, Department of Geological Sciences, University of Florida, USA. The obtained results are expressed in δ notation in reference to the Vienna Pee Dee Belemnite (VPDB) standard. The measurement precision was better than ±0.04‰ for the oxygen isotope and ± 0.02‰ for the carbon isotope. We did not correct the isotope values for vital effects because there is no reliable vital effect correction for *E. clavatum* (Bauch et al., 2004; Ślubowska-Woldengen et al., 2007).

3.6. Mg/Ca analysis and bottom water temperature calculation

A total of 20 to 40 tests of the benthic *Cibicidoides lobatulus* were picked for Mg/Ca analyses from the 100 to 500 μm size fraction. Samples were cleaned prior to the analysis, which included removing clay, metal oxides (with hydrazine), organic matter, and acid leaching (Lea and Boyle, 1991). Mg/Ca values were converted into bottom water temperature (BWT) using the following calibration equation for *Cibicidoides* spp. (Elderfield et al., 2006).

$$\text{Mg/Ca} = 0.90 \times exp.(0.11 \times \text{BWT})$$

3.7. Pigments and biomarkers

For pigment analysis, 3–4 g of frozen sediment sample were placed in

a glass centrifuge tube and left to thaw. The water was removed by centrifugation (2500 rpm, 6 min). The sediment sample was flushed twice with 15 ml acetone, mixed, sonicated (2–3 min), and centrifuged (2500 rpm, 6 min). Next, a liquid–liquid extraction was conducted using a mixture of acetone extract, benzene, and water (15:1:10 *v/v/*v). The benzene layer was transferred to a glass vial, evaporated to dryness in a stream of argon and stored at −20 °C prior to high-performance liquid chromatography (HPLC) analysis. The sediment remaining after extraction was dried at 60 °C and weighed. For HPLC analysis, the evaporated sediment extract was dissolved in acetone and injected (Autosampler, Knauer Optimas, Germany) into a Lichrospher 100RP-18 end-capped column (250 × 4 mm, 5 μm; Merck, Germany) through a guard column (Lichrospher 100RP-18 end-capped, 4 mm × 4 mm; Merck, Germany). Carotenoids and chloropigment-a (e.g., chlorophyll-a and its derivatives) were separated using an HPLC system equipped with a diode-array detector (DAD 2800 Knauer, Germany) by the different mobile phase systems described earlier (Krajewska et al., 2017; Szymczak-Żyła et al., 2017). The pigment content was calculated in nmol per dry sediment weight (d.w).

For biomarker analysis, freeze-dried sediments (~ 4 g) were extracted with a dichloromethane and methanol (2:1 *v*/v) mixture using accelerated solvent extraction (ASE 150; temp 100 °C; 4 cycles; static extraction time: 5 min). Before extraction, the samples were spiked with surrogate standards (9-octylheptadecene, 7-hexylnonadecane, 2-nonadecanone, and androstanol). After extraction, the total lipid extracts were concentrated using rotary evaporation and divided into two subsamples (A and B).

Subsample A was fractionated by solid-phase extraction (SPE) using 1% deactivated silica gel. The fraction containing highly branched isoprenoid (IP_{25}) was eluted with a hexane and dichloromethane (1:1 v/v) mixture, evaporated under a stream of argon, dissolved in a hexane solution, and then analysed using a gas chromatograph coupled to a mass spectrometer detector (GCMS-QP2010 Ultra; Shimadzu). The concentrations of IP_{25} were calculated based on response factors for IP_{25} and the standards according to the procedure described by Belt et al. (2012).

The fraction containing alkenones was eluted with dichloromethane, evaporated under a stream of argon, dissolved in an isooctane solution, and analysed using a gas chromatograph with a flame ionization detector (GC-FID, Shimadzu). The analytes were quantified based on response factors for alkenones and standard.

To determine the total polar steroid fraction, subsample B was saponified with 5 ml of 5% KOH in methanol at 70 °C for 1.5 h before liquid–liquid extraction was conducted in the KOH–methanol extract, chloroform, and water system (1:3:2 v/v/v; three times). The combined chloroform fractions were concentrated by rotary evaporation and derivatized with BSTFA + TMCS (99:1) at 60 °C for 1 h, and the trimethylsilyl derivatives that were dissolved in a hexane solution containing an internal standard (5α-cholestane) were analysed using a gas chromatograph coupled to the mass spectrometer (GC/MS) (GCMS-QP2010 Ultra, Shimadzu). The analytes were identified on the basis of their retention times and mass spectra and quantified based on response factors derived from daily injections of standard mixtures. The following polar steroids were studied: brassicasterol, campesterol, sitosterol, and dinosterol.

The PIP_{25} indices were calculated by combining IP_{25} with different phytoplankton markers for sea ice reconstruction (Müller et al., 2011).

$$P_pIP_{25} = IP_{25}/(IP_{25} + (p \times c))$$

where *p* is the phytoplankton marker concentration (brassicasterol (B) or dinosterol (D)), and c is a balance factor (mean IP_{25} concentration/mean *p* concentration).

The $U^{K'}_{37}$ index was used to estimate the sea surface temperature (SST). The $U^{K'}_{37}$ index was calculated by the following equation (Bendle and Rosell-Melé, 2004).

$$U^{K'}_{37} = C_{37:2}/(C_{37:2} + C_{37:3} + C_{37:4})$$

$U^{K'}_{37}$ values were converted to SSTs using global core-top calibration according to Müller et al. (1998).

$$U^{K'}_{37} = (0.033 \times SST) + 0.044$$

The percentage of $C_{37:4}$ alkenones in the record was calculated according to the following equation (Bendle et al., 2005).

$$C_{37:4} = [C_{37:4}/C_{37:2} + C_{37:3} + C_{37:4}]$$

4. Results

4.1. Core description and lithology

The upper part of the core (0–80 cm) primarily consists of olive-grey (5Y 4/1) fine-grained silty clay. The lower part of the core (80–240 cm) is characterized by brownish-grey (5YR 4/1) finer silty clay with dispersed black pockets of charcoal and occasional shell fragments. CT scans, photographs, and IRD grain distribution reveal five lithological units: IRD with diamictons (18–44 cm), IRD with fine grains (58–84 cm), lamination with coarse grains and IRD (114–142 cm), laminations with fine grains (166–192 cm) and lamination with IRD (194–222 cm).

4.2. Age model

The calibrated ^{14}C dates (Table 1) show that the 2.32 m-long sediment core covers the last ~11,500 kyr BP (Fig. 2). According to the age model, the minimum and maximum sedimentation rates of core HR7 (5.8 and ~ 170 cm kyr^{-1}), are recorded between 5.4 and 3.52 and 0.52 and 0.308 kyr BP, respectively (Fig. 2).

4.3. Foraminifera assemblages and zonation

Fifty-nine benthic foraminifera taxa were identified in the 62 samples collected from sediment core HR7. Calcareous taxa represent approximately 75–100% of the benthic foraminifera. Agglutinated species occur mainly in the upper part of the core (up to ~25%), with decreasing percentages down the core (average ~ 0.5%). Species with >5% relative abundance in at least one sample are shown in Fig. 3. Three species dominate the benthic foraminifera assemblages: *Elphidium clavatum* (12–59%), *Cassidulina reniforme* (9–48%), and *Cibicidoides lobatulus* (2–49%), followed by *Buccella frigida* (0–18%), *Nonionellina labradorica* (~ 2–17%), *Islandiella norcrossi/helenae* (0–54%), *Cribroelphidium albiumbilicatum* (0–5%), and *Stainforthia loeblichi* (0–3%). Planktic foraminifera were very rare throughout the core. Their percentages range between 0 and 5% of the total foraminifera except in the sample dated to ~8.1 kyr BP, where they represent ~8% of total foraminifera.

The downcore succession of four foraminiferal zones was determined using significant changes in the relative abundance and fluxes of the most abundant benthic species, as well as concentrations of total benthic foraminifera. These changes indicate shifts in the environment, which are explained in the following.

4.3.1. Zone I, 11.4–10 kyr BP; 230–205 cm

This zone is characterized by overall low concentrations of benthic and planktic foraminifera. The foraminiferal assemblage is dominated by the benthic calcareous species *C. reniforme, E. clavatum,* and *I. norcrossi/helenae*; agglutinated foraminifera, on the other hand, are almost absent throughout this zone. Abundances of *Nonionellina labradorica* and *B. frigida* were low at the bottom of the zone and gradually increased towards the top of the zone. *Stainforthia loeblichi* also appeared in this zone and decreased towards the top of the zone. The benthic and planktic foraminifera fluxes are extremely low (on average, ~ 2240 and

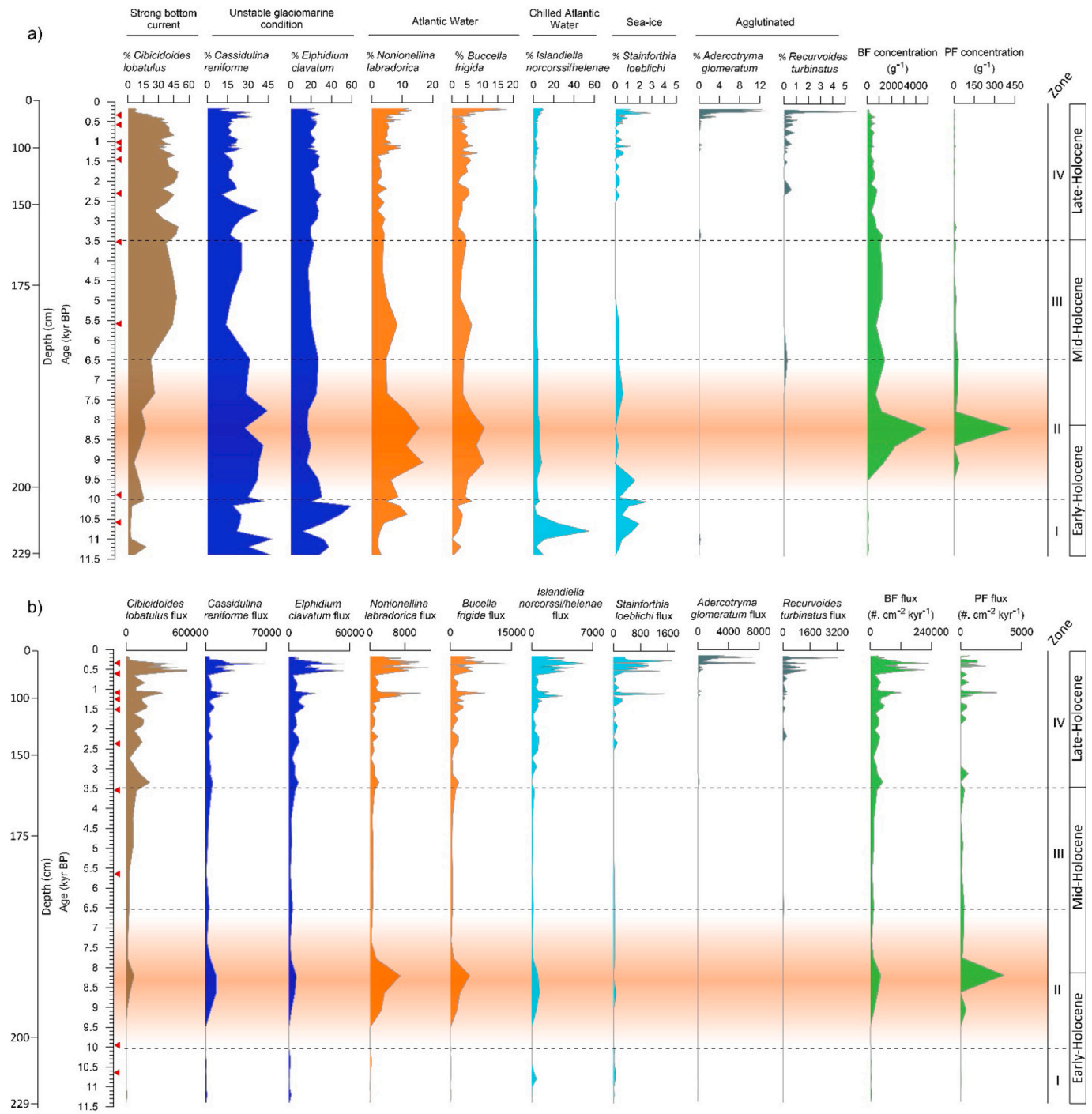

Fig. 3. Panel (a): Relative abundances of selected benthic foraminiferal species and their ecological preferences (see text for explanation). Bottom current indicator - *Cibicides lobatulus* (brown shading); unstable glaciomarine indicators – *Cassidulina reniforme* and *Elphidium clavatum* (blue shading); Atlantic water (AW) indicators – *Nonionellina labradorica and Buccella frigida (*orange *shading); Chilled Atlantic water* indicators – *Islandiella norcrossi/helenae* and sea ice indicator – *Stainforthia loeblichi* (light blue shading); *agglutinated species* – *Adercotryma glomeratum* and *Recurvoides turbinatus* (dark green shading); benthic foraminiferal (BF) and planktic foraminiferal (PF) concentrations – (green shading). Panel (b): Fluxes of selected benthic foraminiferal species; the total flux of benthic foraminifera; the total flux of planktic foraminifera. Foraminiferal zones (zone I-IV) are shown on the right side of the panels. Orange shading stands for the Holocene Thermal Maximum. Red triangles next to the left y-axis indicate radiocarbon dates. (For interpretation of the references to colour in this figure legend, the reader is referred to the web version of this article.)

~ 28 individuals (ind.) cm^{-2} kyr^{-1}, respectively; Fig. 3).

4.3.2. Zone II, 10–6.5 kyr BP; 205–189 cm

This zone is characterized by an increase in the benthic and planktic foraminifera concentrations. As in the previous zone, calcareous benthic foraminifera dominated the entire zone, and the abundances of the agglutinated species were very low. The benthic assemblage is dominated by *N. labradorica* and *B. frigida,* followed by *C. reniforme. Nonionellina labradorica* and *B. frigida* show a maximum abundance between 8.2 and 9 kyr BP, coinciding with the benthic and planktic foraminiferal concentrations and flux maxima (~ 95,300 and 8200 ind. cm^{-2} kyr^{-1}, respectively). The abundance of *E. clavatum* shows a sudden decline at

the bottom of this zone and remains relatively constant throughout. The abundance of *C. lobatulus* gradually increases throughout the zone.

4.3.3. Zone III, 6.5–3.3 kyr BP; 189–169 cm

The benthic assemblage is dominated by *C. lobatulus* and *C. reniforme,* which coincides with a high and stable benthic foraminiferal concentration. The overall abundances of *I. norcrossi/helenae, S. loeblichi,* and agglutinated benthic species remain low throughout the zone. The abundances of *N. labradorica* and *B. frigida* increase at the bottom of the zone and then slightly decrease at the top of the zone. The foraminiferal fluxes remain low throughout the zone.

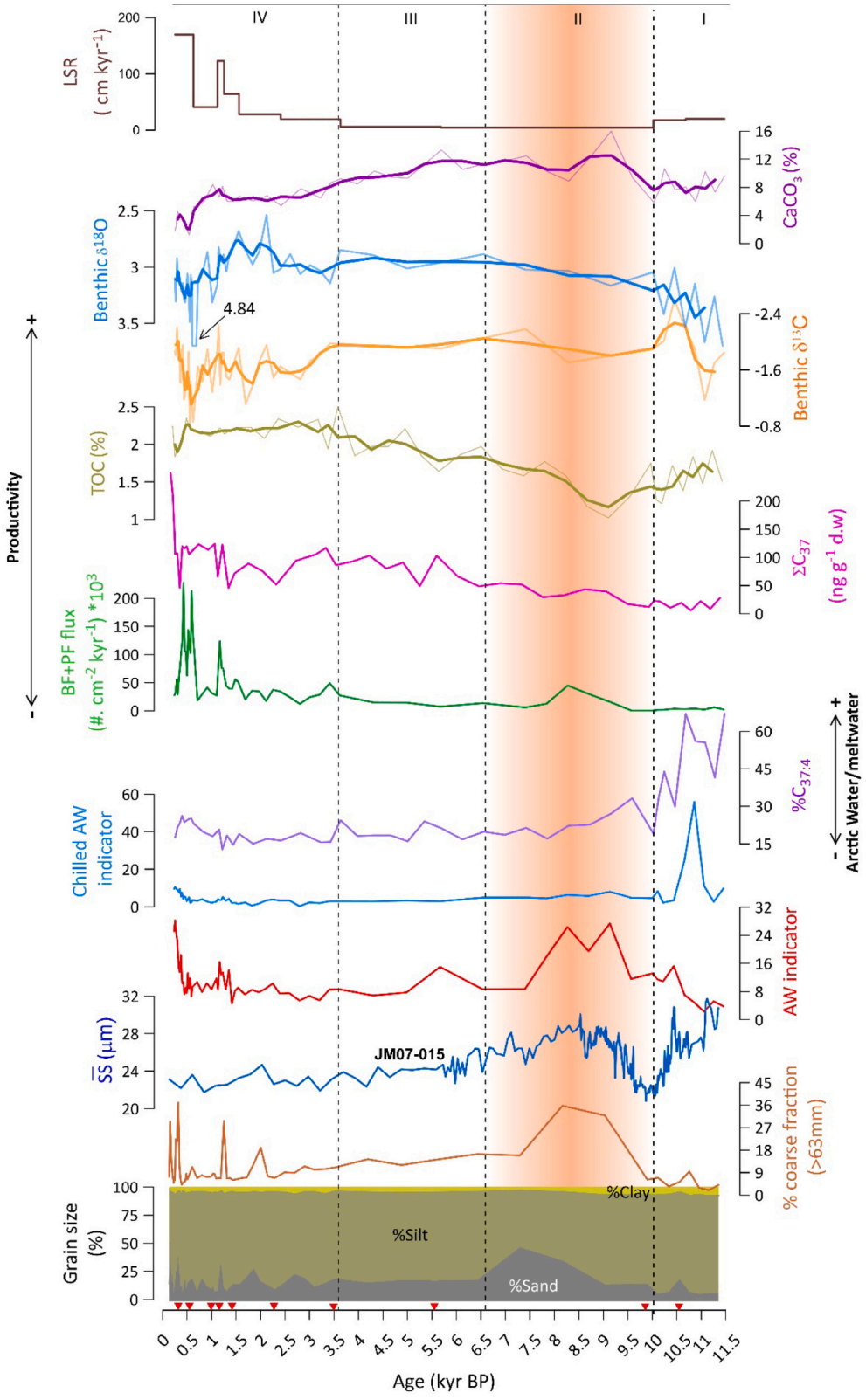

Fig. 4. Combined records of bulk parameters, foraminiferal, alkenone, and benthic stable isotopes from core OCE2019-HR7-GC. From bottom to top: grain size distribution, percentage of coarse-grained sediments (>63 μm), sortable silt (SS) (Sternal et al., 2014), AW indicator, Chilled AW indicator, percentage of $C_{37:4}$ alkenone (%$C_{37:4}$), total foraminiferal flux, total of C_{37} alkenone (ΣC_{37}), total organic carbon (TOC; thin line = raw data, thick line = three-point running average), *benthic foraminiferal* $\delta^{13}C$ and $\delta^{18}O$ (thin line = raw data, thick line = three-point running average), calcium carbonate (%$CaCO_3$; thin line = raw data, thick line = three-point running average) and linear sedimentation rates (LSR). Foraminiferal zones (zone I-IV) are shown on the top of the panels. Orange shading denotes the Holocene Thermal Maximum. Red triangles next to the x-axis indicate radiocarbon dates. (For interpretation of the references to colour in this figure legend, the reader is referred to the web version of this article.)

4.3.4. Zone IV, 3.3–0.14 kyr BP; 169–1 cm

Overall, this zone is characterized by fluctuating abundances of many species and relatively high sedimentation rates. The abundances of *C. lobatulus, C. reniforme, N. labradorica* and *B. frigida* show relatively higher but fluctuating records compared to the previous zones. The overall abundance of *E. clavatum* remains relatively constant, with some small fluctuations. The abundances of agglutinated species are generally low, but the abundances increase at the top of the zone. The benthic foraminiferal concentration declines throughout the zone, and the planktic foraminiferal concentration remains very low, if not almost absent. The benthic flux increases rapidly after ~2.5 kyr BP and reaches its maximum value (~ 227,850 ind. cm^{-2} kyr^{-1}) at 0.33 kyr BP. Apart from a few exceptions, planktic foraminiferal flux is very low throughout the core, with two peaks at ~1.2 and 0.33 kyr BP (~ 8200 and 2970 ind. cm^{-2} kyr^{-1}, respectively).

4.4. Stable isotopes

The stable oxygen isotope values are relatively high (>3‰) and highly variable before ~10 kyr BP (Fig. 4k). Then, the values become low (<3‰) and more stable until ~3.5 kyr BP. The values show slight fluctuations from 3.3 kyr BP to 2.2 kyr BP and then again become highly

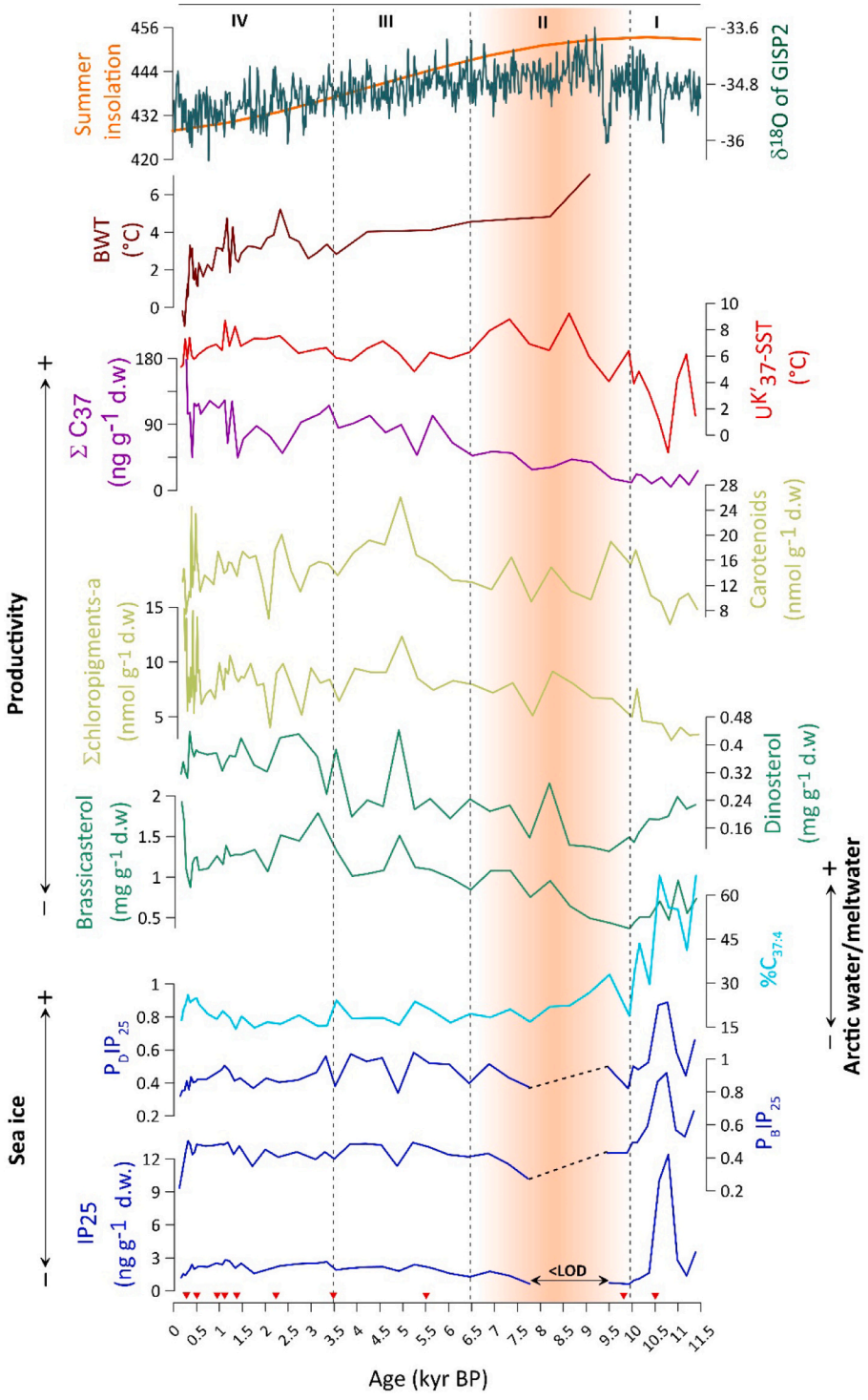

Fig. 5. Combined records of biomarkers and pigments and the correlation of core OCE2019- HR7-GC with the GISP2 ice core. From bottom to top: summary of IP_{25} concentration, calculated P_BIP_{25} and P_DIP_{25} indices, percentage of $C_{37:4}$ alkenone (%$C_{37:4}$), brassicasterol concentration, dinosterol concentration, Σchloropigments-a concentration, carotenoid concentration, total C_{37} alkenone (ΣC_{37}), reconstructed alkenone-derived sea surface temperature ($U^{K'}_{37}$-SST), bottom water temperature (Mg/Ca-BWT), summer insolation at 77°N (black line) and $\delta^{18}O$ of the GISP2 core (orange line) (Grootes et al., 1993). Foraminiferal zones (zone I-IV) are shown on the top of the panels. Orange shading denotes the Holocene Thermal Maximum. Red triangles next to the x-axis indicate radiocarbon dates. LOD: limit of detection. (For interpretation of the references to colour in this figure legend, the reader is referred to the web version of this article.)

variable and start a stepwise increase to reach their maximum of 4.8‰ at 0.52 kyr BP. Benthic $\delta^{13}C$ values gradually decrease from ~11 kyr BP, reaching their lowest value (−2.6‰) at 10.5 kyr BP (Fig. 4j). After that, $\delta^{13}C$ records become more stable up to ~3.3 kyr BP. Between ~2 and 0.14 kyr BP, the values become highly variable and gradually increase until ~0.5 kyr BP and then again decrease to −2.2‰ at 0.19 kyr BP.

4.5. Pigments and biomarkers

The spring sea ice biomarker IP_{25} (average 5.3 ng/g d.w) and the terrigenous biomarkers β-sitosterol (average 0.5 μg/g d.w) and campesterol (average 0.3 μg/g d.w) are high in the base of HR7 (zone I as defined by the foraminifera assemblages) (Figs. 5 and 6). In zone II, the terrigenous biomarkers ß-sitosterol (average 0.34 μg/g d.w) and campesterol (average 0.14 μg/g d.w) are relatively low. Out of the 10 samples analysed in zone II, 4 yielded IP_{25} values (between 9.5 and 7.75

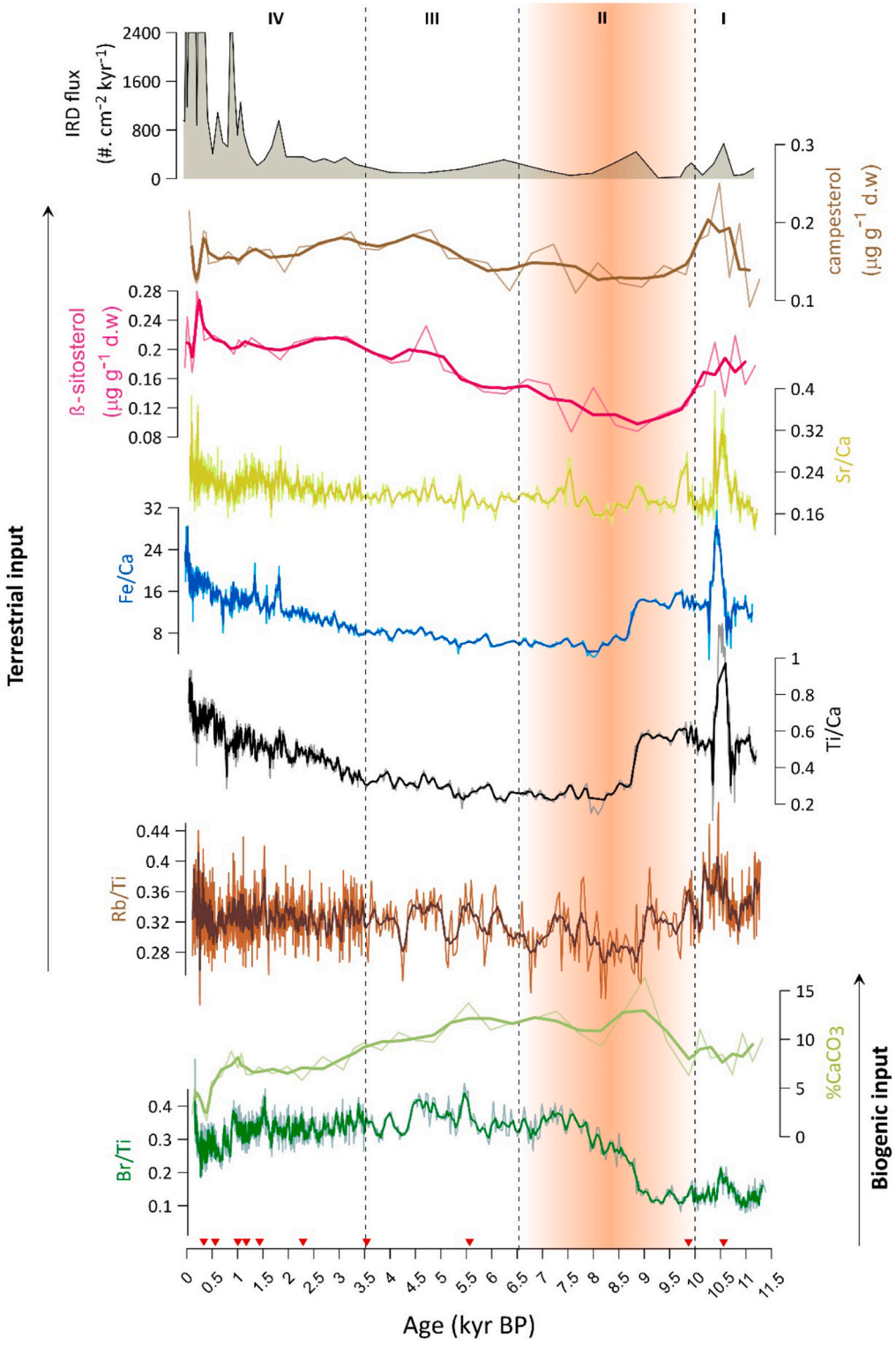

Fig. 6. X-ray fluorescence (XRF) data, % of $CaCO_3$, terrigenous biomarker records, and ice-rafted debris flux (IRD) in core HR7. Foraminiferal zones (zone I-IV) are shown on the top of the panels. Orange shading represents the Holocene Thermal Maximum. Red triangles next to the x-axis indicate radiocarbon dates. Thin line = raw data, thick line = three-point running average. (For interpretation of the references to colour in this figure legend, the reader is referred to the web version of this article.)

kyr BP) absent or, at least, below the instrument detection limit (LOD; <0.5 ng/g d.w), and when present, IP_{25} concentrations are relatively low (average 0.91 ng/g d.w) (Fig. 5). Relatively stable and comparatively high concentrations of IP_{25} are observed in zone III (average 1.98 ng/g d.w) and zone IV (average 2.11 ng/g d.w) compared to zone II. The $C_{37:4}$ percentage maxima occur before 10 kyr BP (zone I) and decline afterwards (Fig. 4f). Concentrations of ΣC_{37} are generally low throughout zone I, followed by a gradual increase before reaching their maximum during zone IV (Fig. 4h). The concentrations of both phytoplankton biomarkers, brassicasterol and dinosterol, show a similar trend in the record. The concentrations are relatively low during zone I and gradually increase throughout the other zones. At the base of zone II, both phytoplankton biomarkers show very low values (10–9.2 kyr BP). The changes to the pigment (carotenoids and Σchloropigments-a) concentrations follow the same patterns as those of the phytoplankton biomarkers throughout the core (Fig. 5). The concentrations are low throughout zone I and then increase gradually. The calculated P_BIP_{25} and P_DIP_{25} indices are high in zone I and vary between 0.19 and 0.93 and 0.17–0.89, respectively (Fig. 5). Both indices show very low values in zone II and relatively low stable records throughout the other zones.

4.6. X-ray fluorescence and IRD

In addition to an overall downcore pattern, the high-resolution XRF record from core HR7 indicates multiple minor events (Fig. 6). Here, we use bulk chemical ratios (Ti/Ca, Fe/Ca, Sr/Ca and Rb/Ti) to identify the source of the sediments, specifically whether they have a marine or terrestrial origin. Additionally, we consider Br (normalized with Ti; Br/Ti) as an indicator of marine biological productivity. Zone I and part of zone II (~ 10–8.8 kyr BP) are characterized by high bulk chemical ratios, while the Br/Ti ratios are low. The maximum increase in bulk chemical ratios is observed in the middle of zone I (between ~11 and 10.5 kyr BP). At the bottom of zone I, the IRD content is relatively low but gradually increases thereafter. Br counts increase throughout zone III, with a slightly elevated IRD content at the beginning of the zone that declines sharply to remain constant throughout the rest of zone III. Sr/Ca ratios are relatively stable throughout zones III and IV. The ratios of Ti/Ca and Fe/Ca show an increasing trend towards zone IV. The IRD content remains constant at the beginning of zone IV but fluctuates throughout the rest of the zone with distinct peaks at ~2.2, 1, and 0.5 kyr BP.

5. Discussion

5.1. Interpretation of palaeoceanography and sedimentary environments

In the Arctic, the benthic foraminiferal species *C. reniforme* is typically found in glaciomarine environments and prefers water temperatures below 2 °C (Łącka and Zajączkowski, 2016). Similarly, *E. clavatum* indicates cold, unstable glaciomarine conditions with highly turbid glacial meltwater input (Hald et al., 1994). The epibenthic species *C. lobatulus* is commonly associated with strong bottom currents (Hald and Korsun, 1997; Steinsund, 1994; Wollenburg and Mackensen, 1998). High abundances of *Stainforthia loeblichi* and *I. norcrossi/helenae* are often considered to be associated with seasonal sea ice cover (Scott et al., 1984; Seidenkrantz, 2013; Steinsund, 1994). Moreover, *I. norcrossi/helenae* has been reported to thrive in areas fed chilled AW (Cage et al., 2021; Lloyd et al., 2007). The calcareous species *N. labradorica* and *B. frigida* are considered indicators of increased productivity and an increased flux of organic matter to the seafloor (Hald and Steinsund, 1996; Wollenburg and Kuhnt, 2000). In addition, the presence of these two species has been linked to relatively warm and saline AW (Lloyd, 2006; Lloyd et al., 2007), which is most abundant in the areas influenced by the WSC near Svalbard and used for paleo interpretations (e.g., Majewski et al., 2009). Since our core location is influenced by the WSC, we interpret the dominance of *N. labradorica* and *B. frigida* in this study as indicative of the presence of nutrient-rich warm saline AW.

Changes in the IRD and grain size distribution indicate variations in ice rafting, terrigenous input, and ocean current strengths and dynamics (Stein et al., 1996). The concentrations of the terrigenous biomarkers ß-sitosterol and campesterol in marine sediment cores are used to indicate terrigenous input, as they are both produced by vascular land plants (Fahl and Stein, 2007; Rontani et al., 2014). The ratios of Ca/Fe, Ca/Ti, and Ca/Sr are frequently used as indicators of the marine biogenic origin of carbon (Vare et al., 2009). Br is used to indicate marine biological productivity and is often associated with high amounts of marine organic carbon (Pruysers et al., 1991; Seki et al., 2019). Therefore, higher Br/Ti ratios suggest a low contribution of terrestrial-originated materials to the sediment (Rothwell and Croudace, 2015). Rb has previously been used as an indicator for environments with terrestrial influence (Møller et al., 2016; Saito, 1998).

The C_{25} isoprenoid lipid biomarker (IP_{25}), is widely used for the estimation of sea-ice coverage (e.g., Belt et al., 2007; Belt et al., 2015; Berben et al., 2014; Pieńkowski et al., 2021). The biosynthesis of this biomarker occurs exclusively within certain diatoms inhabiting the Arctic sea ice (e.g., Brown et al., 2014). Therefore, if IP_{25} is detected in sediment samples, it directly confirms the existence of Arctic sea ice in the past, particularly in seasonally ice-covered regions.

Benthic foraminifera Mg/Ca paleothermometry is a highly effective method for reconstructing paleotemperatures. Mg/Ca ratios offer an advantage over $\delta^{18}O$ paleothermometry because they are not affected by changes in seawater $\delta^{18}O$ resulting from the growth and melting of ice (e.g., Martin et al., 2002). Calibrations of Mg/Ca ratios with temperature have been established for various species of benthic foraminifera across a diverse range of environments (e.g., Barrientos et al., 2018; Elderfield et al., 2006; Evans et al., 2015). Nevertheless, it is important to acknowledge that Mg/Ca exhibits substantial variability, not only within individual species but also between different species (e.g., Segev and Erez, 2006). This high variability strongly indicates a significant influence of physiological factors on the incorporation of magnesium ions (Mg^{2+}) into foraminiferal shells (e.g., Rosenthal et al., 1997; Segev and Erez, 2006).

$U^{K'}_{37}$ indices are widely used as SST proxy in the North Atlantic region (e.g., Łącka et al., 2019; Łącka et al., 2015b; Marchal et al., 2002). However, it is essential to take into consideration the findings of Rosell-Melé (1998), who observed that when the $\%C_{37:4}$ value exceeds 5% of the total $\%C_{37}$ alkenone value and the $U^{K'}_{37}$ index is negative, the calculated temperatures are deemed unreliable. In this study, the calculated $\%C_{37:4}$ values generally exceeded 5%, and therefore an alternative index (Bendle and Rosell-Melé, 2004) was used to estimate SSTs when $\%C_{37:4}$ considerably high (see Section 3.7). The $C_{37:4}$ alkenone is more abundant in the Nordic Seas than at mid to low latitudes compare to the $C_{37:2}$ and $C_{37:3}$ alkenones (e.g., Rosell-Melé, 1998). High percentages of $C_{37:4}$ have previously been used as an indicator for ArW/meltwater, whereas low percentages are associated with AW (Bendle et al., 2005).

5.1.1. Zone I, ~11.4–10 kyr BP - appearance of fresh water and sea ice on the SW Svalbard inner shelf

In zone I, the low ΣC_{37} as well as the low absolute foraminiferal abundances and fluxes coincide with low TOC and Br/Ti (Figs. 4 and 6), altogether indicating that the surface water productivity was low throughout this zone. This is further supported by the relatively low surface productivity proxy records, such as pigments and phytoplankton biomarkers (brassicasterol and dinosterol; Fig. 5). The benthic $\delta^{18}O$ values are highly variable but are decreasing, which suggest that freshening occurred that was likely due to the occasional freshwater inflow from the inner Hornsund fjord.

The base of this zone, between ~11.4 and 11 kyr BP, was characterized by low IP_{25} values and low P_BIP_{25} and P_DIP_{25} values, suggesting less seasonal sea ice at our core site, probably due to the warm surface water conditions reflected by high $U^{K'}_{37}$-SSTs (Fig. 5). High values of %

$C_{37:4}$ between ~11 and 10.2 kyr BP point to a significant influence of cold ArW from the ESC and/or meltwater flux to our study site from the inner Hornsund (Fig. 5). The peak values of Ti/Ca, Fe/Ca, and Sr/Ca and high concentrations of the terrigenous biomarkers campesterol and β-sitosterol could indicate an increase in sediment-laden meltwater overflow, most likely from the inner Hornsund (Fig. 6). The particularly high IP_{25} concentrations and high values of P_BIP_{25} and P_DIP_{25} indices (Fig. 5) that coincide with the occurrences of *S. loeblichi* and other glaciomarine indicators (mostly *E. clavatum*) (Fig. 3) may indicate that the environment was likely affected by sea ice until ~10.2 kyr BP under the influence of cold ArW (see Supplementary Fig. 1; positive correlation between ArW and IP_{25}). $U^{K'}_{37}$-derived SST records show a rapid drop after a short warm period. A relatively high percentage of coarse-grained sediments and an increase in IRD content are observed during this period, suggesting that icebergs were also common over the study site (Figs. 4 and 6).

5.1.2. Zone II, 10–6.5 kyr BP - maximum influence of Atlantic water associated with the Holocene Thermal Maximum

The overall increase in AW indicator species from 10 kyr BP indicates a transition towards ameliorated water mass conditions with more significant AW inflow (Fig. 4d). Both surface and bottom water temperatures reached their maximum between 10 and 6.5 kyr BP, as indicated by UK'_{37}-derived SST and Mg/Ca-derived BWT. The general decrease in $\%C_{37:4}$ points to a weakening of the ArW and/or cold freshwater flow from the inner Hornsund entrainment onto the SW Svalbard shelf. The period between ~9.5 and 7 kyr BP records the interval with the highest advection of warm AW, as suggested by high abundances of the AW indicators that coincide with a peak in benthic and planktic foraminiferal fluxes and concentrations, which indicate warming of the water column (Fig. 3). Notably, the measured IP_{25} concentrations between this period were absent or at least below the LOD, indicating the near absence of sea ice (Fig. 5), also suggested by the absence or very low abundance of *S. loeblichi* (Fig. 3). This further supports the interpretation that maximum surface warming occurred at that time, which is likely associated with the Holocene Thermal Maximum (HTM). The overall stable distribution of *C. reniforme* and low abundance of *E. clavatum* relate to elevated and stable salinities, possibly caused by a weaker ESC, since *C. reniforme* is more tolerant of higher salinities than *E. clavatum* (Hald and Korsun, 1997).

The distinct reduction in phytoplankton biomarker concentrations between ~10 and 9 kyr BP probably suggests short-term deterioration of the surface water conditions. This coincides with rapidly decreasing IP_{25} concentrations and relatively high terrestrial input (Figs. 5 and 6). Therefore, we suggest that the SW Svalbard inner shelf was still affected by considerable sediment-laden meltwater discharge, which may have affected the growth of phytoplankton and ice algae. These surface conditions significantly reduced annual productivity, which is further supported by low foraminiferal fluxes, TOC, pigments, and relatively high benthic $\delta^{13}C$ (Figs. 4 and 5).

The decrease in Ti/Ca, Fe/Ca, and Sr/Ca and low concentrations of terrigenous biomarkers (Fig. 6) observed after ~9 kyr BP coincide with relatively high $CaCO_3$ contents, suggesting that a high amount of marine-originated carbonate was deposited in our study area, which may result from the higher productivity of calcareous organisms such as foraminifera rather than terrestrial input (Andrews and Eberl, 2011; Jackson et al., 2017). Additionally, terrestrial vegetation protruded into tidewater glaciers at the Hornsund mouth (Hansbreen), indicating that glacier terminates were terrestrially grounded before ~8 kyr BP (Oerlemans et al., 2011), and as a result, there was a limited supply of terrestrial materials via icebergs. The reconstructed $U^{K'}_{37}$-derived SST shows an abrupt decrease at the end of the zone (Fig. 5), which is also indicated by the occurrence of the sea ice indicator species *S. loeblichi* (Fig. 3), suggesting the presence of sea ice and generally cooler environmental conditions in SW Svalbard. This is further supported by increasing IP_{25} values, P_BIP_{25}, and P_DIP_{25} indices (Fig. 5).

5.1.3. Zone III, 6.5–3.5 kyr BP - dynamic environment with high productivity

The overall increasing abundance of AW indicator species between 6.5 and 5.5 kyr BP suggests an influx of AW following the later stages of the previous zone (Fig. 4d). Despite the presence of AW during this interval, the sea surface is characterized by sea ice-rich conditions at our study site, as indicated by the continuous occurrence of *S. loeblichi* from the end of the previous zone and relatively high values of IP_{25}, P_BIP_{25}, and P_DIP_{25} (Fig. 5). Mg/Ca-derived BWT and relatively low (<3‰) and constant benthic $\delta^{18}O$ records suggest relatively warm and stable bottom water temperatures at our study site. Records from our productivity-indicating proxies point to a gradual increase in surface water productivity during this interval, most likely due to the growth of ice algae.

A short interval (~5–4.5 kyr BP) of decreasing sea ice at our core site promoted an increase in regional surface productivity rates. A decrease in sea ice is suggested by a slight decrease in IP_{25} concentration, a decrease in P_BIP_{25} and P_DIP_{25} indices, and the absence or minimal occurrence of *S. loeblichi*. The productive surface conditions are further supported by the peaks of the phytoplankton markers, pigments, relatively low benthic $\delta^{13}C$ and high TOC and $CaCO_3$ values. We associate this high productivity to either ice-free summer conditions with a thick photic zone or seasonally fluctuating sea ice margins over the core site. A similar surface condition characterizes the climate shift after 4.5 kyr BP and during a short interval between 6.5 and 5.5 kyr BP. An increase in sea ice at our site is suggested by the elevated concentrations of IP_{25}, as well as the P_BIP_{25} and P_DIP_{25} indices. Decreases in the AW indicator and slight increases in the ArW indicator after 4.5 kyr BP suggest a weakening of AW inflow onto the SW Svalbard shelf (Fig. 4d and f). Hence, we consider the combination of sea ice advance and relatively low AW inflow to our site to most likely indicate the onset of the Neoglacial cooling that occurred at the western Svalbard margin (Svendsen and Mangerud, 1997). Relatively low and decreasing foraminiferal fluxes, decreasing pigment concentrations, and low phytoplankton biomarker concentrations point to restricted phytoplankton productivity, probably due to cold sea ice-rich surface conditions.

5.1.4. Zone IV, 3.5–0.14 kyr BP - neoglacial cooling and the establishment of modern oceanographic conditions

The interval between 3.5 and ~ 2.2 kyr BP is characterized by relatively low foraminiferal fluxes, low TOC, and relatively high benthic $\delta^{13}C$ values (Figs. 4 and 5), suggesting an unfavourable low productivity environment characterized by a cold climate. The reconstructed $U^{K'}_{37}$-derived SST decreased slightly, probably coinciding with the Neoglacial Thermal Minimum (NTM) reported in the Nordic Seas at the same interval (Renssen et al., 2006; Telesinski et al., 2015). Generally, a low abundance of AW indicator species suggests that the AW inflow was further weakened (Fig. 4d). Hence, low bottom current activity is suggested by a drop in *C. lobatulus* along with a slight decrease in the coarse fraction and sand content at our core site (Figs. 3 and 4). In comparison to the later part of the previous zone, the benthic $\delta^{18}O$ tends to increase along with an increase in *E. clavatum*, suggesting relatively cold bottom conditions (Figs. 3 and 4k). This is most likely caused by the continued reduction of AW inflow at our site, which is confirmed by a decrease in Mg/Ca-derived BWT (Fig. 5).

Between 2.3 and ~ 1.5 kyr BP, the increase in abundance of the bottom current indicator *C. lobatulus* coincides with an increase in the coarse fraction and sand content, pointing to strengthened bottom current activity at our study site (Fig. 3). Successively reduced IP_{25} concentrations were accompanied by high reconstructed SSTs, BWTs and low benthic $\delta^{18}O$ records (Figs. 4 and 5). Moreover, a slight increase in AW indicators suggests a strengthening of AW influx to our site. Low $\delta^{13}C$ could be attributed to high surface water productivity, which would have been promoted by relatively low sea ice concentrations and warm surface water conditions (Fig. 4j).

Between 1.5 and 1 kyr BP (450 and 950 CE), we identify a peak

abundance of the AW indicator species and higher SSTs and BWTs at the core site that may have been triggered by a temporarily strengthened WSC. This is also supported by peaks in the coarse fraction and sand content. Similar findings of remarkably warmer SSTs and enhanced influx of AW at ~1.6 kyr BP were also reported in the western Barents Sea continental margins by Sarnthein et al. (2003). The notable increase in foraminiferal fluxes, TOC, phytoplankton biomarkers, and pigments during the last 1 kyr BP coincides with low benthic $\delta^{13}C$ and could be attributed to the high surface water productivity. A high abundance of glaciomarine fauna agrees well with an extraordinary increase in the IRD flux after 1 kyr BP, indicating proximal glacier activity and/or iceberg rafting at our study site. The majority of late Holocene glacial advances were observed to occur predominantly between 1 and 0.5 kyr BP (Farnsworth et al., 2020; Jernas et al., 2013). Moreover, an increase in terrigenous biomarkers could explain the occurrence of icebergs that probably carried terrigenous organic matter, which could be reflected in the high TOC values. The lithological composition of the IRD from a nearby sediment core at Hornsund mouth points to a significant local source of icebergs (Majewski et al., 2009), which are likely derived from Hansbreen, which is the nearest tidewater glacier. A peak of benthic $\delta^{18}O$ was observed between ~0.6 and 0.4 kyr BP (1350 and 1550 CE), suggesting cold bottom water conditions. The increased IRD content and terrigenous biomarkers indicate more iceberg calving and rafting over the study site.

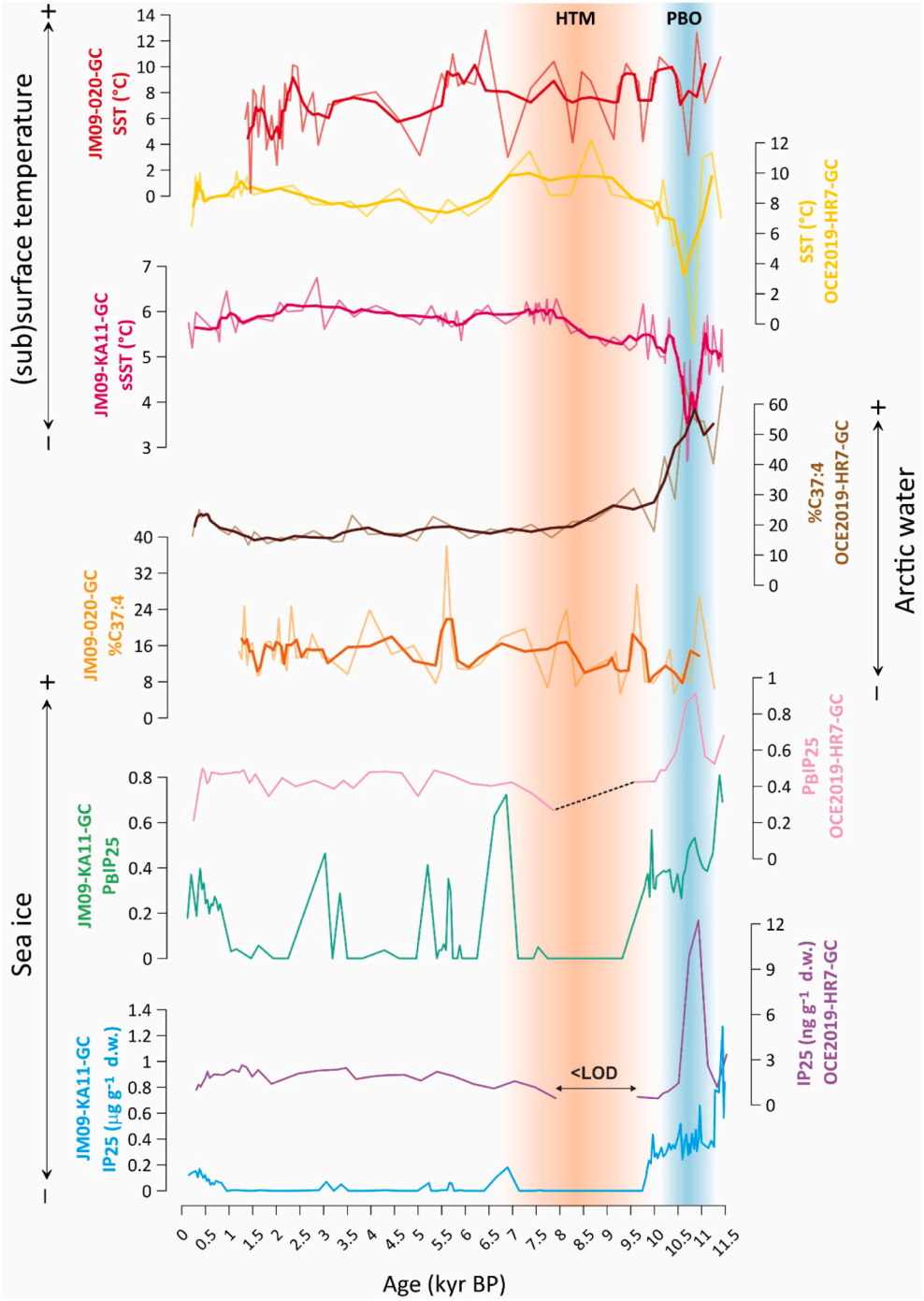

Fig. 7. Comparison between proxies selected from core OCE2019-HR7-GC and proxy records from sediment cores JM09-KA11-GC-GC (Berben et al., 2014) and JM09–020-GC (Łącka et al., 2019) from the western Barents Sea. HTM: Holocene Thermal Maximum (orange shading); PBO: Preboreal Oscillation (light blue shading). LOD: limit of detection. Thick lines imply the three-point running average. (For interpretation of the references to colour in this figure legend, the reader is referred to the web version of this article.)

5.2. Variability in water mass inflow and the environmental response at the SW Svalbard shelf

The multiproxy analysis of sediment core OCE2019-HR07-GC reveals that during the earliest Holocene (~11–10.2 kyr BP), even though it was a period of maximum summer insolation (Fig. 5), the SW Svalbard inner shelf water experienced cold conditions, both at the bottom and at the surface. Increased cold and fresher water flux may have promoted recurrent sea ice cover at our core site, as reflected by maximum occurrences of sea ice indicators (Fig. 5; see also Supplementary Fig. 1, which shows strong negative correlation between $U^{K'}_{37}$-SSTs and IP_{25}). Similar surface conditions have previously been recorded in the western Barents Sea (core JM09-KA11-GC-GC (Berben et al., 2014) and JM09–020-GC (Łącka et al., 2019), Fig. 1), where high $\%C_{37:4}$, IP_{25}, and P_BIP_{25} together point to an inflow of cold fresher ArW and sea ice-rich surface conditions (Fig. 7), most likely related to the initiation of the ESC after the melting of the Svalbard-Barents Ice Sheet (Rasmussen et al., 2007). Several studies described simultaneous and similar cold environmental conditions around the Svalbard margins just after the Younger Dryas (Łącka et al., 2020; Rasmussen et al., 2012; Rasmussen et al., 2014; Skirbekk et al., 2010; Ślubowska-Woldengen et al., 2007). It has been suggested that this was most likely associated with the brief cold interval called the Preboreal Oscillation (Björck et al., 1997). The Arctic Front was shifted westwards from our study site by cold and relatively fresh water, which may have led to the path of the WSC being located farther away from our site (Fig. 8). In addition, the significant changes in the terrigenous signals that we observe in our core (Fig. 6) could also indicate an increase in sediment-laden meltwater overflow from inner Hornsund. Therefore, we conclude that the cold Arctic conditions of the SW Svalbard inner shelf were the result of the combined effect of meltwater overflow from Hornsund fjord and the initiation of the ESC. However, AW may still have reached the inner shelf below a thick cold and fresh thick surface water layer covered by sea ice, as inferred from the presence of chilled AW indicator species (Fig. 3). Consistent with our findings are studies from the outer shelf of SW Svalbard (Storfjorden fan) (Rasmussen et al., 2007) and western Svalbard (Rasmussen et al., 2014; Skirbekk et al., 2010), which indicate the pronounced appearance of AW as a subsurface water mass below the cold ArW layer at the surface.

The first distinct inflow of AW to the SW Svalbard inner shelf during the studied period that induced water column warming was observed at 10 kyr BP and lasted until ~7 kyr BP. This is in agreement with previous studies from the Svalbard shelf and continental slope, which also indicated that the AW exerted a higher influence at the same time (Rasmussen et al., 2012; Rasmussen et al., 2007; Sarnthein et al., 2003; Skirbekk et al., 2010; Ślubowska-Woldengen et al., 2008; Telesiński et al., 2018). The highest reconstructed $U^{K'}_{37}$-derived SST and Mg/Ca-derived BWT indicates that AW dominates the entire water column, and this suggests that the ArW from the ESC and/or cold water from the inner Hornsund on the SW Svalbard inner shelf had minimal influence (Fig. 8; see also Supplementary Fig. 1). The orbitally forced summer insolation was also at a maximum during this period (Fig. 6) (Laskar et al., 2004), which resulted in warmer air and surface water temperatures (Jakobsson et al., 2010) and caused a lowering of the albedo (Stranne et al., 2014). Furthermore, overall warming is also supported by terrestrial records from the Svalbard archipelago, suggesting maximum air temperatures (Farnsworth et al., 2020) and very low sea ice cover in fjords (Allaart et al., 2020). A warming of (sub) surface water by the combined effect of AW advection and increased atmospheric warming (approximately 2 °C higher than present; Birks (1991)) may have strongly reduced sea ice on the SW Svalbard inner shelf, which is reflected in low IP_{25}, P_BIP_{25}, and P_DIP_{25} indices. Similar sea ice-free warm (sub) surface conditions are also explained by lower IP_{25} and P_BIP_{25} and higher reconstructed (sub) surface temperatures in core JM09-KA11-GC (Berben et al., 2014). Berben et al. (2014) further described a gradual and steady increase in the subpolar planktic foraminiferal species *T. quinqueloba* from 10.4 to 7.3 kyr BP. This was interpreted as a change in water masses from Arctic to Atlantic water in the western Barents Sea. According to a modern modelling study (Nilsen et al., 2016), minimal sea ice production along Western Svalbard occurs when AW from the WSC is actively brought towards the fjord mouth by strong southerly wind stress. Furthermore, the study found that the dominant wind direction during the HTM was towards the southeast around Western Svalbard (Sessford et al., 2015).

High bottom current indicator species are associated with high concentrations of coarse-grained sediment. Additionally, the grain size distribution showed a decrease in clay and an increase in sand and silt contents (Fig. 4), indicating that strong bottom currents actively

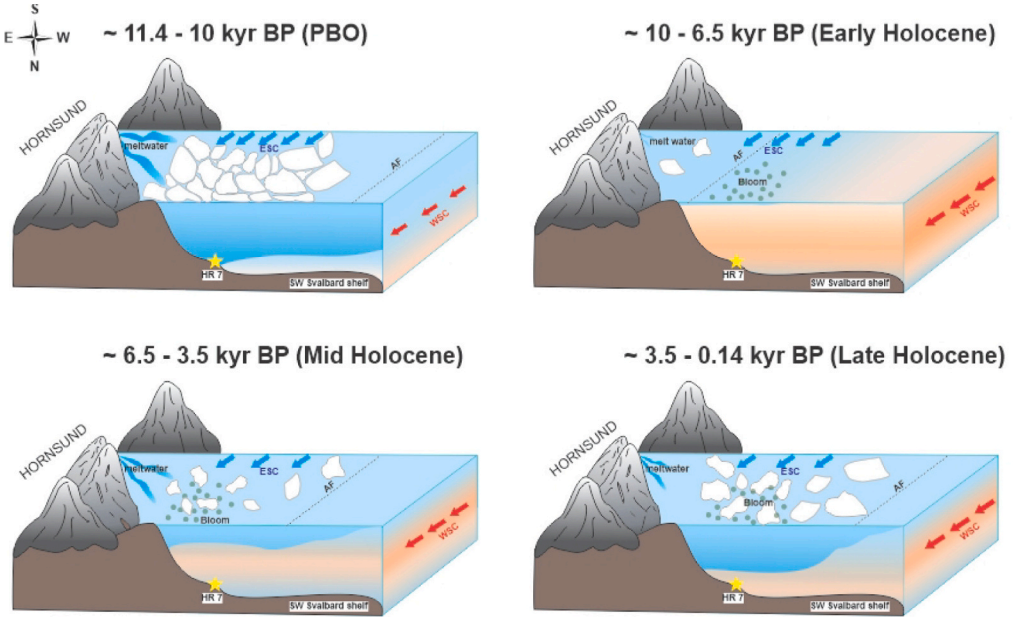

Fig. 8. Time-slice reconstructions of the oceanographic conditions and sea ice cover on the SW Svalbard shelf based on results from core HR07 presented in Fig. 3, Fig. 4, Fig. 5, Fig. 6, and Fig. 7. For the core location, see Fig. 1b. PBO: Preboreal Oscillation; ESC: East Spitsbergen Current; WSC: West Spitsbergen Current; AF: Arctic Front.

winnowed surface sediments from the SW Svalbard inner shelf. This is possibly due to the increased erosive activity of the strengthened WSC, which expanded to the inner shelf (see also Section 6). Palaeo-current reconstructions and data on the mean particle size of sortable silt (SS) (Fig. 4c) from the neighbouring sediment core JM07–015 (Sternal et al., 2014) support this interpretation and suggest increased bottom current velocity during this interval. The sediments from this period were characterized by decreased TOC (Fig. 4i) and terrestrial inputs (Fig. 6), probably related to the extremely active bottom environmental conditions. Moreover, the HTM is also marked by an extremely low sedimentation rate (4.6 cm kyr^{-1}), possibly due to intense near-bottom current activity and limited sediment supply from the melting glaciers. It is suggested that glaciers had already retreated to the glacier bays, supported by lake sediment records in Svalbard suggesting that most glaciers retreated to their minimum extent during the early Holocene (Farnsworth et al., 2020). Thus, we suggest that the interval between 10 and ~ 7 kyr BP represents the latest phase of the HTM in the SW Svalbard inner shelf and infer that icebergs and sea ice rafting occurred less frequently. This was most likely due to the combined effect of higher insolation and the strengthened AW inflow to our study site.

Shortly after 7 kyr BP, our records resemble most other Holocene records from the Svalbard margin, where the weakening of the warm AW signal only affects the bottom waters (Rasmussen et al., 2012; Rasmussen et al., 2007; Ślubowska et al., 2005; Telesiński et al., 2018). The strengthened ESC after ~7 kyr BP (Sarnthein et al., 2003) may have brought some sea ice-rich cold water from the Barents Sea to our site, which is also shown by the clay mineral composition of the nearby core JM07–015 during that period (Sternal et al., 2014). This also coincides with a decrease in SSTs and slight increase in the IRD flux (Figs. 5 and 6) in our records, suggesting an overall increase in sea ice rafting and cold surface conditions in the western Svalbard margins, probably due to ice advance (Hald et al., 2004; Jessen et al., 2010; Ślubowska-Woldengen et al., 2007). Furthermore, the transition starting ~7 kyr BP was also reported around the western Barents Sea-Svalbard regions, where it was marked by a distinct increase in ice rafting (Forwick and Vorren, 2009). Signs of sea ice expansion and surface cooling were also recorded in core JM09-KA11-GC (Fig. 1), which were reflected by the peaks of IP_{25} and P_BIP_{25} (Fig. 7). In particular, a similar distinct surface water cooling was observed at ~7 kyr BP in southern Svalbard (JM09–020-GC; Fig. 7), SW Svalbard (Telesiński et al., 2018), and the eastern Fram Strait at ~7.2 kyr BP (Werner et al., 2013). This suggests that sea ice was likely transported further north along the western Svalbard shelf from the western Barents Sea via the ESC.

A ~ 10% abundance of AW indicator species after 6.5 kyr BP suggests some inflow of AW (Fig. 3), possibly flowing beneath the cold surface water layer. This is consistent with previous Holocene foraminiferal studies in the Svalbard margin (Rasmussen et al., 2012; Rasmussen et al., 2007), western Barents shelf (Sarnthein et al., 2003), and Nordic Seas (Bauch et al., 2001), which suggest that the advection of AW during the HTM lasted until ~6.5 kyr BP. However, at approximately 5.5 kyr BP, a strong ArW signal was recorded in core JM09–020-GC (Fig. 7), suggesting a strengthening of the ESC and inflow of ArW to the western Barents Sea (Łącka et al., 2019). This is also observed in our record, where seasonal sea ice cover conditions and ArW signals are suggested by an increase in ArW and sea ice indicators (Fig. 7). The relatively high IRD fluxes in our record (Fig. 6) have also been linked to ice rafting, which is consistent with the glacier advance in western Spitsbergen at approximately 5.5 kyr BP (Fjeldskaar et al., 2018; Skirbekk et al., 2010). The SST record shows cooling in surface water masses, further suggesting the presence of a cold ArW layer at our site (Fig. 7). Mg/Ca-derived BWT suggests that bottom conditions were relatively cooler at this interval than during the HTM. Furthermore, it is possible that cold dense water from brine rejection during sea ice formation penetrated the bottom of the SW Svalbard shelf. Therefore, cooler bottom conditions, potentially due to the mixing of AW with cold dense brine water and/or meltwater from the inner Hornsund produced the transformed Atlantic water (TAW).

From 3.4 kyr BP onwards, it appears that there was a continuous but relatively weak inflow of AW onto the southwest Svalbard inner shelf, likely below the cold surface water layer with sea ice, as reflected by low UK'_{37}-derived SST and high IP_{25} concentration. The brief and temporary reduction in the AMOC at approximately 3 kyr BP (Telesinski et al., 2015) due to low orbital forcing may have been related to a weakening of AW advection to the SW Svalbard shelf. Similarly, a weak inflow of AW as a bottom water mass to northern Svalbard was also reported by Bartels et al. (2017). Fresher cold water from the inner Hornsund and/or ESC formed a cold, low salinity sea ice-rich surface layer, possibly created a strong pycnocline that might have separated the subsurface warm AW from the cold surface layer. The sea ice indicators suggest the presence of typical seasonal to marginal sea ice conditions, but there is no clear trend, except for a slight increase compared to the preceding interval. Similarly, in the western Barents Sea (core JM09-KA11-GC, Fig. 1), the formation of seasonal sea ice was suggested by peaks in IP_{25} (Fig. 7). This is in accordance with records from the eastern Fram Strait, where the occurrence of sea ice followed the Neoglacial Cooling (Müller et al., 2012).

Despite this, our data show two periods of substantially warmer SSTs and BWTs at the SW Svalbard shelf at approximately 2.3 and 1.5 kyr BP, likely as a result of the short-term expansion of warm AW in the entire water column, which was triggered by a temporarily strengthened WSC. Furthermore, similar (sub) surface warming was also observed in both cores JM09-KA11-GC and JM09–020-GC in the western Barents Sea (Fig. 7). This is also supported by previous findings from eastern Svalbard (Pawłowska et al., 2020), the western Barents shelf (Sarnthein et al., 2003) and the Fram Strait (Müller et al., 2012), where two similar intervals with warmer conditions appeared at approximately 2.2 and 1.6 kyr BP. Our records indicate an active bottom current-induced erosive condition at that time, as reflected in the high abundance of *C. lobatulus*, high coarse fraction, and increased sand content (Fig. 6) . A notable increase in SS in the nearby core JM07–015 (Fig. 4c) also reflects an increase in near-bottom current speed during this interval (Sternal et al., 2014). The increased erosive activity on the western Svalbard shelf during the late Holocene (~2.3–1.5 kyr BP) was identified by different studies (e.g., Andruleit et al. (1996)), but the source of the hydrodynamic energy was not completely revealed. Here we suggest that the sudden increase in hydrodynamic energy at our study site was most likely due to (1) the expansion of the WSC onto the SW Svalbard shelf and/or (2) the increased vertical circulation in the water column due to excessive heat loss to the atmosphere(e.g., Kuhlbrodt et al., 2007) from AW under open water conditions (reflected in significantly reduced IP_{25}; Fig. 5), which caused strong bottom currents that eroded surface sediments. Another explanation for the strong bottom current could be the formation of dense water as a result of cooling below large icebergs. An increase in IRD content during this interval suggests increased iceberg rafting over the study area, further supporting this explanation (Fig. 6).

6. Conclusions

The presented multiproxy data offer novel insights into the Holocene palaeoceanographic evolution of the SW Svalbard shelf. Sea ice and ArW indicators suggest extensive sea ice cover and cold ArW derived from ESC between 11 and 10.2 kyr BP. The warmest period of the Holocene on the SW Svalbard shelf occurred from 10 to 7 kyr BP, which is associated with an enhanced AW influx via the WSC. This promoted sediment erosion and very low sea ice cover. After 7 kyr BP, the AW advection weakened, and the surface became cooler, which promoted the formation of sea ice. From 6.5 to 3.5 kyr BP, the environment was dynamic, with icebergs, the rafting of sea ice and cold surface conditions likely due to ice advancement. A consistent yet weak influx of warm AW to the SW Svalbard inner shelf continued during the late Holocene (after 3.5), which likely occurred beneath a cold surface water layer covered by sea ice. The study also presents evidence for two distinct intervals

(~2.3 and 1.5 kyr BP) characterized by elevated temperatures, increased erosive activity, and the expansion of warm AW throughout the entire water column, likely due to a temporary strengthening of the West Spitsbergen Current and increased vertical circulation in the southwest Svalbard inner shelf.

Author contributions

DD: Conceptualization, Formal analysis, Investigations, Writing – original draft, Visualization; MŁ: Conceptualization, Formal analysis, Investigations, Writing – review and editing, Project Management, Funding acquisition; NS: Writing – review and editing; MS-Z: Formal analysis, Writing – review and editing; MK: Formal analysis; AW: Writing – review and editing; SDS: Writing – review and editing, Funding acquisition; MHS: Formal analysis, Writing – review and editing; MZ: Cruise planning and leading, Conceptualization, Investigations, Writing – review and editing, Supervision, Project Management, Funding acquisition.

Data availability.

All data presented in this paper are available in the open database for Earth and Environmental Science PANGAEA.

Declaration of competing interest

The authors declare no competing interests.

Data availability

Data presented in this paper have been uploaded to PANGAEA

Acknowledgments

The research was financially supported by the Norwegian Financial Mechanism for 2014-2021, project no 2019/34/H/ST10/00682. MZ, MŁ, and MS-Ż contributions were supported by National Science Centre in Poland through project 2019/33/B/ST10/00297. SDS is supported by the European Research Council (ERC) under the European Union's Horizon 2020 Research and Innovation Programme (grant agreement No 818449). We would like to thank Agnieszka Kujawa for helping with the foraminiferal analysis and Prof. Simon T. Belt and Dr. Lukas Smik (University of Plymouth, UK) for providing reference sediment and standards for IP_{25} analyses. We also extend our gratitude to the R/V Oceania crew who helped during sediment core retrieval.

Appendix A. Supplementary data

Supplementary data to this article can be found online at https://doi.org/10.1016/j.gloplacha.2023.104213.

References

Aagaard, K., Greisman, P., 1975. Toward new mass and heat budgets for the Arctic Ocean. J. Geophys. Res. 80, 3821–3827.

Allaart, L., Müller, J., Schomacker, A., Rydningen, T.A., Håkansson, L., Kjellman, S.E., Mollenhauer, G., Forwick, M., 2020. Late Quaternary glacier and sea-ice history of northern Wijdefjorden, Svalbard. Boreas 49, 417–437.

Andersen, C., Koç, N., Jennings, A., Andrews, J.T., 2004. Nonuniform response of the major surface currents in the Nordic Seas to insolation forcing: Implications for the Holocene climate variability. Paleoceanography 19. https://doi.org/10.1029/2002PA000873.

Andrews, J.T., Eberl, D., 2011. Surface (sea floor) and near-surface (box cores) sediment mineralogy in Baffin Bay as a key to sediment provenance and ice sheet variations. Can. J. Earth Sci. 48, 1307–1328.

Andruleit, H., Freiwald, A., Schäfer, P., 1996. Bioclastic carbonate sediments on the southwestern Svalbard shelf. Mar. Geol. 134, 163–182.

Barrientos, N., Lear, C.H., Jakobsson, M., Stranne, C., O'Regan, M., Cronin, T.M., Gukov, A.Y., Coxall, H.K., 2018. Arctic Ocean benthic foraminifera Mg/Ca ratios and global Mg/Ca-temperature calibrations: new constraints at low temperatures. Geochim. Cosmochim. Acta 236, 240–259.

Bartels, M., Titschack, J., Fahl, K., Stein, R., Seidenkrantz, M.-S., Hillaire-Marcel, C., Hebbeln, D., 2017. Atlantic Water advection vs. glacier dynamics in northern Spitsbergen since early deglaciation. Clim. Past 13, 1717–1749.

Bauch, H.A., Erlenkeuser, H., Spielhagen, R.F., Struck, U., Matthiessen, J., Thiede, J., Heinemeier, J., 2001. A multiproxy reconstruction of the evolution of deep and surface waters in the subarctic Nordic seas over the last 30,000yr. Quat. Sci. Rev. 20, 659–678.

Bauch, H.A., Erlenkeuser, H., Bauch, D., Mueller-Lupp, T., Taldenkova, E., 2004. Stable oxygen and carbon isotopes in modern benthic foraminifera from the Laptev Sea shelf: implications for reconstructing proglacial and profluvial environments in the Arctic. Mar. Micropaleontol. 51, 285–300.

Belt, S.T., Massé, G., Rowland, S.J., Poulin, M., Michel, C., LeBlanc, B., 2007. A novel chemical fossil of palaeo sea ice: IP25. Org. Geochem. 38, 16–27.

Belt, S.T., Brown, T.A., Rodriguez, A.N., Sanz, P.C., Tonkin, A., Ingle, R., 2012. A reproducible method for the extraction, identification and quantification of the Arctic Sea ice proxy IP 25 from marine sediments. Anal. Methods 4, 705–713.

Belt, S.T., Cabedo-Sanz, P., Smik, L., Navarro-Rodriguez, A., Berben, S.M.P., Knies, J., Husum, K., 2015. Identification of paleo Arctic winter sea ice limits and the marginal ice zone: optimised biomarker-based reconstructions of late Quaternary Arctic Sea ice. Earth Planet. Sci. Lett. 431, 127–139.

Bendle, J., Rosell-Melé, A., 2004. Distributions of UK^{37} and $UK^{37'}$ in the surface waters and sediments of the Nordic Seas: implications for paleoceanography. Geochem. Geophys. Geosyst. 5 (11), Q11013.

Bendle, J., Rosell-Melé, A., Ziveri, P., 2005. Variability of unusual distributions of alkenones in the surface waters of the Nordic seas. Paleoceanography 20, PA2001.

Berben, S.M.P., Husum, K., Cabedo-Sanz, P., Belt, S.T., 2014. Holocene sub-centennial evolution of Atlantic water inflow and sea ice distribution in the western Barents Sea. Clim. Past 10, 181–198.

Berger, A., Loutre, M.-F., 1991. Insolation values for the climate of the last 10 million years. Quat. Sci. Rev. 10, 297–317.

Birks, H.H., 1991. Holocene vegetational history and climatic change in West Spitsbergen-plant macrofossils from Skardtjørna, an Arctic lake. The Holocene 1, 209–218.

Birks, C.J.A., KoÇ, N., 2008. A high-resolution diatom record of late-Quaternary Sea-surface temperatures and oceanographic conditions from the eastern Norwegian Sea. Boreas 31, 323–344.

Björck, S., Rundgren, M., Ingolfsson, O., Funder, S., 1997. The Preboreal oscillation around the Nordic Seas: terrestrial and lacustrine responses. J. Quatern. Sci. Publ. Quatern. Res. Assoc. 12, 455–465.

Brown, T.A., Belt, S.T., Tatarek, A., Mundy, C.J., 2014. Source identification of the Arctic Sea ice proxy IP25. Nat. Commun. 5, 4197.

Cage, A.G., Pienkowski, A.J., Jennings, A., Knudsen, K.L., Seidenkrantz, M.S., 2021. Comparative analysis of six common foraminiferal species of the genera Cassidulina, Paracassidulina, and Islandiella from the Arctic-North Atlantic domain. J. Micropalaeontol. 40, 37–60.

Calvo, E., Grimalt, J., Jansen, E., 2002. High resolution $U^{37}K$ sea surface temperature reconstruction in the Norwegian Sea during the Holocene. Quat. Sci. Rev. 21, 1385–1394.

Cohen, J., Screen, J.A., Furtado, J.C., Barlow, M., Whittleston, D., Coumou, D., Francis, J., Dethloff, K., Entekhabi, D., Overland, J., Jones, J., 2014. Recent Arctic amplification and extreme mid-latitude weather. Nat. Geosci. 7, 627–637.

Devendra, D., Łącka, M., Telesiński, M.M., Rasmussen, T.L., Sztybor, K., Zajączkowski, M., 2022. Paleoceanography of the Northwestern Greenland Sea and return Atlantic current evolution, 35–4 kyr BP. Glob. Planet. Chang. 217, 103947.

Ebbesen, H., Hald, M., Eplet, T.H., 2007. Lateglacial and early Holocene climatic oscillations on the western Svalbard margin, European Arctic. Quat. Sci. Rev. 26, 1999–2011.

Elderfield, H., Yu, J., Anand, P., Kiefer, T., Nyland, B., 2006. Calibrations for benthic foraminiferal Mg/ca paleothermometry and the carbonate ion hypothesis. Earth Planet. Sci. Lett. 250, 633–649.

Evans, D., Erez, J., Oron, S., Müller, W., 2015. Mg/Ca-temperature and seawater-test chemistry relationships in the shallow-dwelling large benthic foraminifera Operculina ammonoides. Geochim. Cosmochim. Acta 148, 325–342.

Fahl, K., Stein, R., 2007. Biomarker records, organic carbon accumulation, and river discharge in the Holocene southern Kara Sea (Arctic Ocean). Geo-Mar. Lett. 27, 13–25.

Farnsworth, W.R., Allaart, L., Ingolfsson, O., Alexanderson, H., Forwick, M., Noormets, R., Retelle, M., Schomacker, A., 2020. Holocene glacial history of Svalbard: Status, perspectives and challenges. Earth Sci. Rev. 208.

Fetterer, F., Fowler, C., 2006. U.S. National Ice Center Arctic Sea Ice Charts and Climatologies in Gridded Format, 1972–2007, Version 1 [Data Set]. National Snow and Ice Data Center, Boulder, Colorado USA. https://doi.org/10.7265/N5X34VDB.

Fjeldskaar, W., Bondevik, S., Amantov, A., 2018. Glaciers on Svalbard survived the Holocene thermal optimum. Quat. Sci. Rev. 199, 18–29.

Forwick, M., Vorren, T.O., 2009. Late Weichselian and Holocene sedimentary environments and ice rafting in Isfjorden, Spitsbergen. Palaeogeogr. Palaeocl. 280, 258–274.

Grootes, P.M., Stuiver, M., White, J., Johnsen, S., Jouzel, J., 1993. Comparison of oxygen isotope records from the GISP2 and GRIP Greenland ice cores. Nature 366, 552–554.

Hald, M., Korsun, S., 1997. Distribution of modern benthic foraminifera from fjords of Svalbard, European Arctic. J. Foraminiferal Res. 27, 101–122.

Hald, M., Steinsund, P., 1996. Benthic foraminifera and carbonate dissolution in the surface sediments of the Barents and Kara Seas. Ber. Polarforsch. 212, 285–307.

Hald, M., Steinsund, P.I., Dokken, T., Korsun, S., Polyak, L., Aspeli, R., 1994. Recent and Late Quaternary Distribution of Elphidium Excavatumf. Clavatumin arctic seas, Cushman Foundation for Foraminiferal Research, p. 141.

Hald, M., Ebbesen, H., Forwick, M., Godtliebsen, F., Khomenko, L., Korsun, S., Ringstad Olsen, L., Vorren, T.O., 2004. Holocene paleoceanography and glacial history of the West Spitsbergen area, Euro-Arctic margin. Quat. Sci. Rev. 23, 2075–2088.
Hald, M., Andersson, C., Ebbesen, H., Jansen, E., Klitgaard-Kristensen, D., Risebrobakken, B., Salomonsen, G.R., Sarnthein, M., Sejrup, H.P., Telford, R.J., 2007. Variations in temperature and extent of Atlantic Water in the northern North Atlantic during the Holocene. Quat. Sci. Rev. 26, 3423–3440.
Heaton, T.J., Köhler, P., Butzin, M., Bard, E., Reimer, R.W., Austin, W.E., Ramsey, C.B., Grootes, P.M., Hughen, K.A., Kromer, B., 2020. Marine20—the marine radiocarbon age calibration curve (0–55,000 cal BP). Radiocarbon 62, 779–820.
Jackson, R., Carlson, A.E., Hillaire-Marcel, C., Wacker, L., Vogt, C., Kucera, M., 2017. Asynchronous instability of the North American-Arctic and Greenland ice sheets during the last deglaciation. Quat. Sci. Rev. 164, 140–153.
Jakobsson, M., Long, A., Ingólfsson, Ó., Kjær, K.H., Spielhagen, R.F., 2010. New insights on Arctic Quaternary climate variability from palaeo-records and numerical modelling. Quat. Sci. Rev. 29, 3349–3358.
Jernas, P., Klitgaard Kristensen, D., Husum, K., Wilson, L., Koç, N., 2013. Palaeoenvironmental changes of the last two millennia on the western and northern Svalbard shelf. Boreas 42, 236–255.
Jessen, S.P., Rasmussen, T.L., Nielsen, T., Solheim, A., 2010. A new late Weichselian and Holocene marine chronology for the western Svalbard slope 30,000–0 cal years BP. Quat. Sci. Rev. 29, 1301–1312.
Knies, J., Pathirana, I., Cabedo-Sanz, P., Banica, A., Fabian, K., Rasmussen, T.L., Forwick, M., Belt, S.T., 2016. Sea-ice dynamics in an Arctic coastal polynya during the past 6500 years. Arktos 3.
Krajewska, M., Szymczak-Żyła, M., Kowalewska, G., 2017. Algal pigments in Hornsund (Svalbard) sediments as biomarkers of Arctic productivity and environmental conditions. Pol. Polar Res. 38, 423–443.
Kuhlbrodt, T., Griesel, A., Montoya, M., Levermann, A., Hofmann, M., Rahmstorf, S., 2007. On the driving processes of the Atlantic meridional overturning circulation. Rev. Geophys. 45.
Łącka, M., Zajączkowski, M., 2016. Does the recent pool of benthic foraminiferal tests in fjordic surface sediments reflect interannual environmental changes? The resolution limit of the foraminiferal record. Ann. Soc. Geol. Pol. 86, 59–71.
Łącka, M., Zajączkowski, M., Forwick, M., Szczuciński, W., 2015a. Late Weichselian and Holocene palaeoceanography of Storfjordrenna, southern Svalbard. Clim. Past 11, 587–603.
Łącka, M., Pawłowska, J., Zajączkowski, M., 2015b. New methods in the reconstruction of arctic marine palaeoenvironments. Imp. Clim. Changes Mar. Environ. 127–148.
Łącka, M., Cao, M., Rosell-Melé, A., Pawłowska, J., Kucharska, M., Forwick, M., Zajączkowski, M., 2019. Postglacial paleoceanography of the western Barents Sea: implications for alkenone-based sea surface temperatures and primary productivity. Quat. Sci. Rev. 224, 105973–105986.
Łącka, M., Michalska, D., Pawlowska, J., Szymanska, N., Szczucinski, W., Forwick, M., Zajaczkowski, M., 2020. Multiproxy paleoceanographic study from the western Barents Sea reveals dramatic Younger Dryas onset followed by oscillatory warming trend. Sci. Rep. 10, 15667–15674.
Laskar, J., Robutel, P., Joutel, F., Gastineau, M., Correia, A., Levrard, B., 2004. A long-term numerical solution for the insolation quantities of the Earth. Astron. Astrophys. 428, 261–285.
Lea, D.W., Boyle, E.A., 1991. Barium in planktonic foraminifera. Geochim. Cosmochim. Acta 55, 3321–3331.
Lloyd, J.M., 2006. Modern distribution of benthic foraminifera from Disko Bugt, West Greenland. J. Foramin Res. 36, 315–331.
Lloyd, J.M., Kuijpers, A., Long, A., Moros, M., Park, L.A., 2007. Foraminiferal reconstruction of mid-to late-Holocene Ocean circulation and climate variability in Disko Bugt, West Greenland. The Holocene 17, 1079–1091.
Loeblich Jr., A.R., Tappan, H., 2015. Foraminiferal Genera and their Classification. Springer.
Loeng, H., 1991. Features of the physical oceanographic conditions of the Barents Sea. Polar Res. 10, 5–18.
Lubinski, D.J., Polyak, L., Forman, S.L., 2001. Freshwater and Atlantic water inflows to the deep northern Barents and Kara seas since ca 13 14Cka. Quat. Sci. Rev. 20, 1851–1879.
Majewski, W.S., Zczuciński, W., Zajączkowski, M., 2009. Interactions of Arctic and Atlantic water-masses and associated environmental changes during the last millennium, Hornsund (SW Svalbard). Boreas 38, 529–544.
Mangerud, J., Bondevik, S., Gulliksen, S., Karin Hufthammer, A., Høisæter, T., 2006. Marine 14C reservoir ages for 19th century whales and molluscs from the North Atlantic. Quat. Sci. Rev. 25, 3228–3245.
Marchal, O., Cacho, I., Stocker, T.F., Grimalt, J.O., Calvo, E., Martrat, B., Shackleton, N., Vautravers, M., Cortijo, E., van Kreveld, S., Andersson, C., Koç, N., Chapman, M., Sbaffi, L., Duplessy, J.-C., Sarnthein, M., Turon, J.-L., Duprat, J., Jansen, E., 2002. Apparent long-term cooling of the sea surface in the Northeast Atlantic and Mediterranean during the Holocene. Quat. Sci. Rev. 21, 455–483.
Martin, P.A., Lea, D.W., Rosenthal, Y., Shackleton, N.J., Sarnthein, M., Papenfuss, T., 2002. Quaternary deep sea temperature histories derived from benthic foraminiferal Mg/ca. Earth Planet. Sci. Lett. 198, 193–209.
Møller, H.S., Jensen, K.G., Kuijpers, A., Aagaard-Sørensen, S., Seidenkrantz, M.S., Prins, M., Endler, R., Mikkelsen, N., 2016. Late-Holocene environment and climatic changes in Ameralik Fjord, Southwest Greenland: evidence from the sedimentary record. The Holocene 16, 685–695.
Müller, P.J., Kirst, G., Ruhland, G., Von Storch, I., Rosell-Melé, A., 1998. Calibration of the alkenone paleotemperature index U37K′ based on core-tops from the eastern South Atlantic and the global ocean (60 N-60 S). Geochim. Cosmochim. Acta 62, 1757–1772.
Müller, J., Wagner, A., Fahl, K., Stein, R., Prange, M., Lohmann, G., 2011. Towards quantitative sea ice reconstructions in the northern North Atlantic: a combined biomarker and numerical modelling approach. Earth Planet. Sci. Lett. 306, 137–148.
Müller, J., Werner, K., Stein, R., Fahl, K., Moros, M., Jansen, E., 2012. Holocene cooling culminates in sea ice oscillations in Fram Strait. Quat. Sci. Rev. 47, 1–14.
Nilsen, F., Skogseth, R., Vaardal-Lunde, J., Inall, M., 2016. A simple Shelf Circulation Model: Intrusion of Atlantic Water on the West Spitsbergen Shelf. J. Phys. Oceanogr. 46, 1209–1230.
Oerlemans, J., Jania, J., Kolondra, L., 2011. Application of a minimal glacier model to Hansbreen, Svalbard. Cryosphere 5, 1–11.
Pawłowska, J., Łącka, M., Kucharska, M., Pawlowski, J., Zajączkowski, M., 2020. Multiproxy evidence of the Neoglacial expansion of Atlantic Water to eastern Svalbard. Clim. Past 16, 487–501.
Pieńkowski, A.J., Husum, K., Belt, S.T., Ninnemann, U., Köseoğlu, D., Divine, D.V., Smik, L., Knies, J., Hogan, K., Noormets, R., 2021. Seasonal Sea ice persisted through the Holocene thermal Maximum at 80 N. Commun. Earth Environ. 2, 124.
Pruysers, P.A., de Lange, G.J., Middelburg, J.J., 1991. Geochemistry of eastern Mediterranean sediments: primary sediment composition and diagenetic alterations. Mar. Geol. 100, 137–154.
Rasmussen, T.L., Thomsen, E., 2015. Palaeoceanographic development in Storfjorden, Svalbard, during the deglaciation and Holocene: evidence from benthic foraminiferal records. Boreas 44, 24–44.
Rasmussen, T.L., Thomsen, E., Ślubowska, M.A., Jessen, S., Solheim, A., Koç, N., 2007. Paleoceanographic evolution of the SW Svalbard margin (76°N) since 20,000 14C yr BP. Quat. Res. 67, 100–114.
Rasmussen, T.L., Forwick, M., Mackensen, A., 2012. Reconstruction of inflow of Atlantic Water to Isfjorden, Svalbard during the Holocene: Correlation to climate and seasonality. Mar. Micropaleontol. 94-95, 80–90.
Rasmussen, T.L., Thomsen, E., Skirbekk, K., Ślubowska-Woldengen, M., Klitgaard Kristensen, D., Koç, N., 2014. Spatial and temporal distribution of Holocene temperature maxima in the northern Nordic seas: interplay of Atlantic-, Arctic- and polar water masses. Quat. Sci. Rev. 92, 280–291.
Renssen, H., Goosse, H., Muscheler, R., 2006. Coupled climate model simulation of Holocene cooling events: oceanic feedback amplifies solar forcing. Clim. Past 2, 79–90.
Risebrobakken, B., Dokken, T., Smedsrud, L.H., Andersson, C., Jansen, E., Moros, M., Ivanova, E.V., 2011. Early Holocene temperature variability in the Nordic Seas: the role of oceanic heat advection versus changes in orbital forcing. Paleoceanography 26, PA4206.
Rontani, J.-F., Charrière, B., Sempéré, R., Doxaran, D., Vaultier, F., Vonk, J.E., Volkman, J.K., 2014. Degradation of sterols and terrigenous organic matter in waters of the Mackenzie Shelf, Canadian Arctic. Org. Geochem. 75, 61–73.
Rosell-Melé, A., 1998. Interhemispheric appraisal of the value of alkenone indices as temperature and salinity proxies in high-latitude locations. Paleoceanography 13, 694–703.
Rosenthal, Y., Boyle, E., Slowey, N., 1997. Temperature control on the incorporation of Mg, Sr, F and Cd into benthic foraminiferal shells from Little Bahama Bank: prospects for thermocline paleoceanography. Geochim. Cosmochim. Acta 61, 3633–3643.
Rothwell, R.G., Croudace, I.W., 2015. Micro-XRF studies of sediment cores: a perspective on capability and application in the environmental sciences. Micro-XRF Stud. Sedim. Cores. Springer 1–21.
Saito, S., 1998. Major and trace element geochemistry of sediments from East Greenland Continental rise: an implication for sediment provenante and source area weathering. In: Proceedings-Ocean Drilling Program Scientific Results. CITESEER, pp. 19–28.
Saloranta, T.M., Haugan, P.M., 2004. Northward cooling and freshening of the warm core of the West Spitsbergen current. Polar Res. 23, 79–88.
Saloranta, T.M., Svendsen, H., 2001. Across the Arctic front west of Spitsbergen: high-resolution CTD sections from 1998–2000. Polar Res. 20, 177–184.
Sarnthein, M., Van Kreveld, S., Erlenkeuser, H., Grootes, P.M., Kucera, M., Pflaumann, U., Schulz, M., 2003. Centennial-to-millennial-scale periodicities of Holocene climate and sediment injections off the western Barents shelf, 75 degrees N. Boreas 32, 447–461.
Scott, D.B., Mudie, P.J., Vilks, G., Younger, D.C., 1984. Latest Pleistocene—Holocene paleoceanographic trends on the continental margin of eastern Canada: Foraminiferal, dinoflagellate and pollen evidence. Mar. Micropaleontol. 9, 181–218.
Screen, J.A., Simmonds, I., 2010. The central role of diminishing sea ice in recent Arctic temperature amplification. Nature 464, 1334–1337.
Segev, E., Erez, J., 2006. Effect of Mg/Ca ratio in seawater on shell composition in shallow benthic foraminifera. Geochem. Geophys. Geosyst. 7.
Seidenkrantz, M.-S., 2013. Benthic foraminifera as palaeo sea-ice indicators in the subarctic realm – examples from the Labrador Sea–Baffin Bay region. Quat. Sci. Rev. 79, 135–144.
Seki, A., Tada, R., Kurokawa, S., Murayama, M., 2019. High-resolution Quaternary record of marine organic carbon content in the hemipelagic sediments of the Japan Sea from bromine counts measured by XRF core scanner. In: Progress in Earth and Planetary Science, 6.
Serreze, M.C., Barry, R.G., 2011. Processes and impacts of Arctic amplification: a research synthesis. Glob. Planet. Chang. 77, 85–96.
Serreze, M., Barrett, A., Stroeve, J., Kindig, D., Holland, M., 2009. The emergence of surface-based Arctic amplification. Cryosphere 3, 11–19.
Sessford, E.G., Strzelecki, M.C., Hormes, A., 2015. Reconstruction of Holocene patterns of change in a High Arctic coastal landscape, Southern Sassenfjorden, Svalbard. Geomorphology 234, 98–107.

Skirbekk, K., Kristensen, D.K., Rasmussen, T.L., Koç, N., Forwick, M., 2010. Holocene climate variations at the entrance to a warm Arctic fjord: evidence from Kongsfjorden trough, Svalbard. Geol. Soc. Lond., Spec. Publ. 344, 289–304.
Skogseth, R., Haugan, P., Jakobsson, M., 2005. Watermass transformations in Storfjorden. Cont. Shelf Res. 25, 667–695.
Ślubowska, M.A., Koç, N., Rasmussen, T.L., Klitgaard-Kristensen, D., 2005. Changes in the flow of Atlantic water into the Arctic Ocean since the last deglaciation: evidence from the northern Svalbard continental margin, 80°N. Paleoceanography 20, PA4014.
Ślubowska-Woldengen, M., Rasmussen, T.L., Koç, N., Klitgaard-Kristensen, D., Nilsen, F., Solheim, A., 2007. Advection of Atlantic Water to the western and northern Svalbard shelf since 17,500calyr BP. Quat. Sci. Rev. 26, 463–478.
Ślubowska-Woldengen, M., Koç, N., Rasmussen, T.L., Klitgaard-Kristensen, D., Hald, M., Jennings, A.E., 2008. Time-slice reconstructions of ocean circulation changes on the continental shelf in the Nordic and Barents Seas during the last 16,000 cal yr B.P. Quat. Sci. Rev. 27, 1476–1492.
Stein, R., Nam, S.-I., Grobe, H., Hubberten, H., 1996. Late Quaternary glacial history and short-term ice-rafted debris fluctuations along the East Greenland continental margin. Geol. Soc. Lond., Spec. Publ. 111, 135–151.
Steinsund, P., 1994. Benthic Foraminifera in Surface Sediments of the Barents and Kara Seas: Modern and Late Quaternary Applications. University of Tromsø, Tromsø, p. 111.
Sternal, B., Szczuciski, W., Forwick, M., ZajĄCzkowski, M., Lorenc, S., Przytarska, J., 2014. Postglacial variability in near-bottom current speed on the continental shelf off South-West Spitsbergen. J. Quat. Sci. 29, 767–777.
Stranne, C., Jakobsson, M., Björk, G., 2014. Arctic Ocean perennial sea ice breakdown during the early Holocene Insolation Maximum. Quat. Sci. Rev. 92, 123–132.
Stuiver, M., Reimer, P.J., Reimer, R.W., 2022. CALIB 8.2 [WWW program]. at. http://calib.org. Accessed 2022-2-25.
Svendsen, J.I., Mangerud, J., 1997. Holocene glacial and climatic variations on Spitsbergen, Svalbard. The Holocene 7, 45–57.
Szymczak-Żyła, M., Krajewska, M., Winogradow, A., Zaborska, A., Breedveld, G.D., Kowalewska, G., 2017. Tracking trends in eutrophication based on pigments in recent coastal sediments. Oceanologia 59, 1–17.
Telesinski, M.M., Bauch, H.A., Spielhagen, R.F., Kandiano, E.S., 2015. Evolution of the central Nordic Seas over the last 20 thousand years. Quat. Sci. Rev. 121, 98–109.
Telesiński, M.M., Przytarska, J.E., Sternal, B., Forwick, M., Szczuciński, W., Łącka, M., Zajączkowski, M., 2018. Palaeoceanographic evolution of the SW Svalbard shelf over the last 14 000 years. Boreas 47, 410–422.
Vare, L.L., Massé, G., Gregory, T.R., Smart, C.W., Belt, S.T., 2009. Sea ice variations in the Central Canadian Arctic Archipelago during the Holocene. Quat. Sci. Rev. 28, 1354–1366.
Werner, K., Spielhagen, R.F., Bauch, D., Hass, H.C., Kandiano, E., 2013. Atlantic Water advection versus sea-ice advances in the eastern Fram Strait during the last 9 ka: Multiproxy evidence for a two-phase Holocene. Paleoceanography 28, 283–295.
Wollenburg, J.E., Kuhnt, W., 2000. The response of benthic foraminifers to carbon flux and primary production in the Arctic Ocean. Mar. Micropaleontol. 40, 189–231.
Wollenburg, J.E., Mackensen, A., 1998. Living benthic foraminifers from the Central Arctic Ocean: faunal composition, standing stock and diversity. Mar. Micropaleontol. 34, 153–185.